SDUST2023VGGA: A Global Ocean Vertical Gradient of Gravity Anomaly Model Determined from Multidirectional Data from Mean Sea Surface

Ruichen Zhou[1,2,3], Jinyun Guo[1,*], Shaoshuai Ya[1], Heping Sun[2], and Xin Liu[1]

[1]College of Geodesy and Geomatics, Shandong University of Science and Technology, Qingdao 266590, China
[2]State Key Laboratory of Precision Geodesy, Innovation Academy for Precision Measurement Science and Technology, Chinese Academy of Sciences, Wuhan 430077, China
[3]University of Chinese Academy of Sciences, Beijing 100049, China
[*]Correspondence: jinyunguo1@126.com

Abstract. Satellite altimetry is a vital tool for global ocean observation, providing critical insights into ocean gravity and its ~~gradient~~gradients. Over the past six years, satellite data from various space agencies have nearly tripled, facilitating the development of high-precision ocean gravity anomaly and ocean vertical gradient of gravity anomaly (VGGA) models. This study constructs a global ocean VGGA model named SDUST2023VGGA using ~~multi-directional mean sea surface data~~multidirectional Mean Sea Surface (MSS). To address computational ~~resource~~ limitations, the global ocean is divided into ~~ten~~ 72 sub-regions. In each sub-region, the DTU21 ~~Mean Sea Surface (MSS)~~ MSS model and the CNES-CLS22 Mean Dynamic Topography (MDT) model are used to derive the geoid. To mitigate the influence of long-wavelength signals on the calculations, the study subtracts the long-wavelength geoid derived from the XGM2019e 2190 gravity field model from the ~~original geoid~~ geoid (full-wavelength), resulting in a residual geoid (short-wavelength). To ensure the accuracy of the VGGA calculations, a weighted least-squares method is employed using residual geoid data from a $17' \times 17'$ area surrounding the computation point. This approach effectively accounts for the ~~actual~~ real ocean environment, thereby enhancing the precision of the calculation results. After combining the VGGA models for all sub-regions, the model's reliability is validated against the SIO V32.1 VGGA (named curv) model. The comparison between the ~~VGGA~~ SDUST2023VGGA and the SIO V32.1 model shows a residual mean is -0.08 Eötvös (E) and the RMS is 8.50 E, ~~indicating a high degree of consistency across the~~ demonstrating high consistency on a global scale. Analysis of the differences reveals that the advanced data processing and modeling strategies employed in the DTU21 MSS model enable SDUST2023VGGA to maintain stable performance across varying ocean depths, unaffected by ocean dynamics. The effective use of ~~multi-directional mean sea surface data~~ multidirectional MSS allows for the detailed capture of ocean gravity field information embedded in the MSS model. Analysis across diverse ocean regions demonstrates that the SDUST2023VGGA model successfully reveals the internal structure and mass distribution of the seafloor. The SDUST2023VGGA ~~dataset~~ model is freely available at https://doi.org/10.5281/zenodo.14177000 (Zhou et al., 2024).

1 Introduction

Gradients of gravity are the partial derivatives of the gravity vector components along the three axes of a Cartesian coordinate system. They describe spatial variations in the Earth's gravitational field~~in space~~, reflecting changes in both magnitude and direction. By enhancing high-frequency signals, gradients of gravity provide a ~~more~~ detailed representation of subsurface density structures (Mortimer, 1977). This capability makes them valuable for accurately ~~depicting~~ characterizing the spatial structure of field sources, understanding the Earth's internal structure, and identifying the location and depth of density variations (Romaides et al., 2001; Oruç, 2011; Panet et al., 2014). Consequently, gradients of gravity play a crucial role in geophysical exploration and ocean gravity field studies (Butler, 1984).

In recent years, ~~ocean~~ the vertical gradient of gravity (VGG) ~~have~~ has demonstrated significant potential across various disciplines, particularly in earthquake monitoring, underwater navigation, and ocean exploration. Fuchs et al. (2013) utilized ~~gradient data~~ gravity gradients from the GOCE satellite to detect substantial gravitational field changes resulting from the 2011 Tohoku earthquake in Japan, ~~finding that the~~ revealing that the observed gravity signal exceeded model predictions. This study ~~underscored~~ highlighted the sensitivity and spatial correlation capabilities of ~~gradient of gravity~~ gravity gradient technology in capturing seismic signals. Similarly, Wang et al. (2023) proposed a wavelet-transform-based regional matching method~~that advanced~~, advancing the application of gradients of gravity in underwater navigation ~~,~~ and significantly improving matching accuracy~~and demonstrating~~. This work demonstrated the technology's practicality and precision. Furthermore, ~~gradient~~ gradients of gravity inversion has proven to be ~~important~~ a powerful tool in ocean exploration. Wan et al. (2023) combined satellite altimetry data with neural network techniques to predict global ocean depths, showcasing the broad applicability of gradients of gravity in oceanographic studies. Additionally, research by Kim and Wessel (2011) demonstrated that extracting short-wavelength information from satellite altimetry data effectively reveals the mass distribution of seafloor fracture zones and seamounts, ~~offering~~ providing new insights into geological structure analysis. These studies illustrate the diverse applications of gradients of gravity in earthquake monitoring, underwater navigation, bathymetry, and geological structure research.

As the application of ~~gradient~~ gradients of gravity technology expands and gravity field theory evolves rapidly, ~~gradient~~ gradients of gravity measurement techniques have seen continuous improvement (DiFrancesco et al., 2009; Stray et al., 2022; van der Meijde et al., 2015). However, measuring mobile gravity gradients remains costly, and achieving comprehensive global ocean coverage continues to be a challenge. The GOCE satellite, equipped with electrostatic accelerometer-based gravity gradiometers, provides global gravity data (Silvestrin et al., 2012; Rummel et al., 2011; Marks et al., 2013). Despite this, its resolution is limited in providing high-precision local ~~gradient~~ gradients of gravity data (Novák et al., 2013).

In contrast, satellite altimetry technology has matured significantly and is now widely used to construct gravity potential models (Zingerle et al., 2020; Pavlis et al., 2012), ~~mean sea surface~~ Mean Sea Surface (MSS) models ~~(Andersen et al., 2023; ?; Yuan et al., 2~~ ~~, mean dynamic topography~~ (Andersen et al., 2023; Yuan et al., 2023), Mean Dynamic Topography (MDT) models (Knudsen et al., 2021; Jousset et al., 2023, 2022), ocean gravity models ~~(Sandwell and Smith, 2009; Sandwell et al., 2014; Garcia et al., 2014; Hwang~~ (Sandwell and Smith, 2009; Sandwell et al., 2014; Garcia et al., 2014; Hwang et al., 1998; Hao et al., 2023; Zhu et al., 2022; Li et al., 202 , ocean gradient of gravity models (Bouman et al., 2011; Sandwell, 1992; Annan et al., 2024; Zhou et al., 2023), seafloor to-

pography models (Smith and Sandwell, 1997; GEBCO Bathymetric Compilation Group 2024, 2024; Hu et al., 2020), sea level studies (Schwatke et al., 2015; Vignudelli et al., 2019; Ablain et al., 2017), and monitoring changes in terrestrial lake water levels (Hwang et al., 2016; Sulistioadi et al., 2015). Among these, the ~~mean sea surface (MSS) is~~ MSS represents a relatively stable sea level~~, determined~~ . It is calculated by averaging instantaneous sea surface height ~~data~~ measurements from satellite altimetry over a specific time period (Andersen and Knudsen, 2009). ~~MSS is crucial in both geodesy and physical oceanography, where it is extensively~~ It is widely used to analyze ocean circulation, detect mesoscale eddies, assess sea level ~~variations~~changes, determine geoid undulations, and identify crustal deformation~~(?).~~ . Additionally, the MSS has broad applications ~~across~~ in geodesy, oceanography, geophysics, and climatology. In geodesy, it serves as a global ~~sea level reference~~reference for sea level, aiding in the study of geoid variations and ~~assisting in determining the precise positions~~ helping to determine the precise locations of Earth's surface features and vertical crustal movements. In oceanography, the MSS is employed to study global ocean circulation, sea surface temperature, and changes in sea ice (Fu and Cheney, 1995; Vermeer and Rahmstorf, 2009; Skourup et al., 2017). In geophysics, it contributes to the analysis of the Earth's gravity field and seismic activity (Melini and Piersanti, 2006). In climatology, sea level data are fundamental for understanding the relationship between global sea level changes and climate change ~~(Vermeer and Rahmstorf, 2009; ?)~~(Vermeer and Rahmstorf, 2009).

To fully extract the detailed ocean ~~gravity field~~ VGGA information embedded in the DTU21 MSS model, this study proposes a method for constructing a global ~~vertical gradient of gravity anomaly (VGGA) model using multi-directional~~ VGGA model using multidirectional MSS data. Sect. ~~2~~ 2 introduces the DTU21 MSS model and outlines the criteria for selecting additional datasets. Sect. ~~3~~ 3 comprises two subsections: Sect. ~~3.1~~ 3.1 outlines the strategy for partitioning the global ocean ~~regions~~into sub-regions, describing how the ocean is divided ~~into multiple areas~~ based on geographic features and oceanographic dynamics. Sect. ~~3.2~~ 3.2 presents a newly developed method aimed at maximizing the extraction of ocean ~~gravity field~~ VGGA information from the DTU21 MSS model, thereby enhancing the effectiveness of gravity field data extraction. Sect. ~~4~~ 4 evaluates the constructed model and assesses its reliability, while Sect. ~~5~~ 5 discusses the factors influencing the model's construction results and key findings observed during the process. ~~After addressing data availability in Sect. 6, a summary of the model construction methods and results is provided in Sect. 7.~~ Sect. 6 presents the conclusions.

2 Research Data

2.1 DTU21MSS

The DTU21 MSS model was developed by the National Space Institute of the Technical University of Denmark (DTU) (Andersen et al., 2023). The dataset is publicly available at https://data.dtu.dk/articles/dataset/DTU21_Mean_Sea_Surface/19383221. This model utilizes satellite altimetry data from multiple missions, including Topex/Poseidon, the Jason series, CryoSat-2, and SARAL/AltiKa, providing high-precision sea surface observations from January 1, 1993, to December 31, 2012.

To enhance the precision and resolution of the data, the DTU21 MSS model employs a new processing chain that incorporates ~~updated~~ advanced filtering and editing techniques. Compared to its predecessors, DTU15MSS and DTU18MSS, which were constructed using 1 Hz satellite altimetry data, DTU21 MSS is based on 2 Hz data, significantly improving its accuracy. The

integration of satellite altimetry data with advanced retracking techniques and the application of the Parks-McClellan filtering algorithm ~~in developing the~~ during the development of the DTU21 MSS model enabled enhanced resolution in the 10–40 km wavelength range, significantly improving accuracy in polar and coastal regions.

The DTU21 ~~mean sea surface~~ MSS dataset is provided in a gridded format. By combining data from multiple satellite sources and utilizing advanced processing methods, the DTU21 model delivers high spatial resolution and precision on a global scale, making it a reliable resource for oceanographic and Earth science research.

2.2 CNES-CLS22 MDT

To extract geoid information from the ~~mean sea surface (MSS)~~ MSS model, a ~~Mean Dynamic Topography (MDT)~~ MDT model is required. The CNES-CLS22 MDT, with a resolution of $7.5' \times 7.5'$, was derived by integrating data from satellite altimetry, the GRACE and GOCE gravity missions, and in-situ oceanographic measurements, such as drifter velocities, high-frequency radar velocities, and salinity-temperature profiles (Jousset et al., 2023). The dataset is accessible at https://www.aviso.altimetry.fr/en/data/products/auxiliary-products/mdt/mdt-global-cnes-cls.html.

Compared to its predecessor, CNES-CLS18 MDT, the CNES-CLS22 MDT demonstrates significant improvements in high-latitude regions. It offers broader coverage and eliminates artifacts, primarily due to the use of a new initial estimate that incorporates the CNES-CLS22 MSS and the GOCO06s geoid model. Additionally, optimal filtering techniques, such as Lagrangian filtering in coastal areas, were applied to further enhance accuracy.

~~Selecting~~ The selection of the CNES-CLS22 MDT ensures minimal correlation with the DTU21 MSS (Knudsen et al., 2022, 2021), making it more effective for extracting detailed ocean gravity field information embedded in the ~~mean sea surface~~ MSS model. This choice enhances the credibility of the VGGA model developed in this study.

2.3 XGM2019e

A highly accurate Earth gravity field model is essential for applying the remove-restore method. In this study, the reference gravity field model XGM2019e_2190 was selected due to its widespread use in geoscience research and practical applications. The model is available from the International Centre for Global Earth Models (ICGEM) at https://icgem.gfz-potsdam.de/home (Ince et al., 2019).

XGM2019e is a comprehensive global gravity field model, complete to degree and order 5399, offering a half-wavelength resolution of approximately 4 kilometers. In this study, the XGM2019e_2190 model, truncated to degree and order 2190, is utilized. It is primarily based on the GOCO06s satellite gravity field model, supplemented by a 15-minute terrestrial gravity dataset and a 1-minute enhanced gravity dataset provided by the U.S. National Geospatial-Intelligence Agency (Zingerle et al., 2020). The integration of satellite and ground-based gravity data ensures high precision in both large-scale and local gravity field representations, making XGM2019e suitable for detailed geophysical studies, including oceanography, tectonics, and geoid determination.

The model's high resolution and accuracy are critical for improving the reliability of the VGGA model developed in this study. By using XGM2019e_2190 in the remove-restore process, the long-wavelength components of the gravity field are efficiently removed, allowing for focused extraction of the high-frequency VGGA from the ~~mean sea surface~~ MSS model.

2.4 SIO V32.1

Given the significant challenges in obtaining in-situ measurements of VGGAs over the oceans, this study utilized the SIO V32.1 dataset, derived from satellite altimetry data, to validate its results. The SIO V32.1 dataset is a high-precision, high-resolution global ocean dataset that includes models for the VGGA, gravity anomaly, and the north-south and east-west components of the deflection of the vertical (DOV) (Garcia et al., 2014). The latest version, V32.1, also incorporates an MSS model.

The SIO V32.1 dataset has been widely used in geophysical and oceanographic studies due to its ability to provide detailed gravity field information over oceanic regions, which is difficult to achieve using traditional measurement techniques. The combination of satellite altimetry data and advanced processing algorithms allows for high spatial resolution, making this dataset particularly useful for detecting fine-scale oceanic structures, including seamounts, fracture zones, and variations in seafloor topography. Using the SIO V32.1 dataset for cross-validation ensures the robustness and reliability of the VGGA model developed in this study.

2.5 GEBCO Bathymetric Model

To evaluate the performance of the SDUST2023VGGA model ~~in~~ under different bathymetric conditions, this study ~~employed~~ employs the General Bathymetric Chart of the Oceans (GEBCO) bathymetric model~~as reference data. The GEBCO model~~ . The first objective is to assess the performance of SDUST2023VGGA in various seafloor topographies. The second objective is to evaluate the correlation between the GEBCO model and SDUST2023VGGA, particularly examining whether VGGAs can explain seafloor topography. The GEBCO model is widely recognized in the field of geosciences for its detailed representation of the seafloor topography of the world's oceans ~~. The model~~ and is available on the GEBCO project website (https://www.gebco.net/data_and_products/gridded_bathymetry_data/).

The GEBCO bathymetric model combines ship-based bathymetric surveys and satellite-derived altimetric data. It provides a global, high-resolution depiction of seafloor depth. The current version, GEBCO2024, has a spatial resolution of 15 arc-seconds, which is approximately equivalent to 450 meters at the equator. This high resolution allows for the identification of various seafloor features such as seamounts, trenches, and ridges, thereby supporting a wide range of geophysical and oceanographic studies.

3 Research methods

3.1 Global zoning strategy

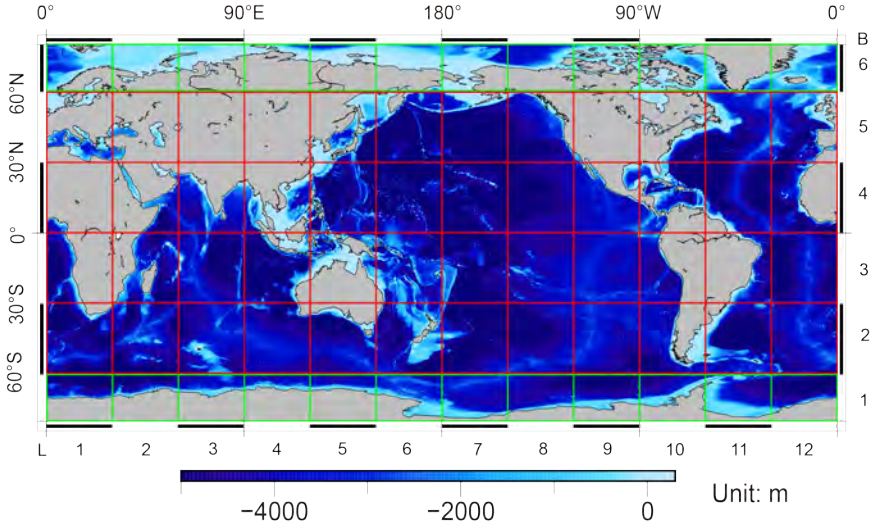

Figure 1. Global oceanic partition strategy using 30° × 30° and 30° × 20° grids based on the ~~Partition-Build-Merge~~ regionalized global modeling approach. ~~The sub-regions~~ Sub-regions are labeled as L1 to L12 (horizontal) and B1 to B6 (vertical) for identification.

~~To address the limitations of computational resources, this study employed a partition-build-merge strategy~~ To overcome computational limitations, a regionalized global modeling approach was adopted. The global ocean was divided into ~~several~~ multiple sub-regions, each computed independently ~~before merging the results into a comprehensive model. For regions between latitudes~~ and then merged into a unified global model. Between 60° S and 60° N, each sub-region was defined as a 30° × 30° ~~. For regions outside~~ grid. Beyond these latitudes, ~~sub-regions were set~~ the grid size was adjusted to 30° × 20° to account for the unique geographic characteristics of high-latitude ~~areas. For easier analysis, the~~ regions. As shown in Figure 1, sub-regions were systematically labeled~~, as shown in Figure 1~~: horizontally, they were labeled L1 to L12 starting from 0° longitude and moving eastward~~, sub-regions were labeled L1 to L12; vertically, starting at~~ ; vertically, they were labeled B1 to B6 starting from 80° S latitude and moving northward~~, they were labeled B1 to B6~~.

To mitigate edge effects during ~~calculations, a 2° boundary extension was applied to~~ derivative calculations, each sub-region ~~. For sub-regions with a standard size of~~ was extended with an excluded margin. For standard 30° × 30° sub-regions, the MSS and MDT models were expanded to ~~cover an area of~~ a 32° × 32° area to include these margins. After constructing the VGGA model for the extended ~~32° × 32° area, the 2° boundary was removed~~region, the excluded margins were clipped, leaving the core 30° × 30° sub-region, as ~~shown~~ illustrated in Figure 2. This clipping strategy ~~ensured that boundary information was preserved~~ preserved critical boundary information during derivative calculations, effectively reducing edge effects and ~~improving~~ enhancing the accuracy of the final model. ~~Extending~~ By temporarily extending sub-region boundaries ~~before trimming minimized~~ where possible, the loss of ~~critical data at the edges, thereby ensuring more reliable results when computing the VGGA~~ important edge data was minimized, ensuring reliable results in VGGA computations. This approach

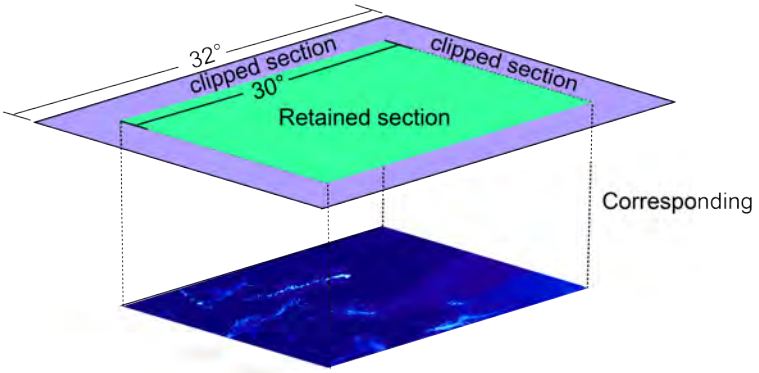

Figure 2. Clipping strategy ~~with a 2° boundary extension~~ to mitigate edge effects. ~~Each~~ The example illustrates a 30° × 30° sub-region ~~was~~ expanded to 32° × 32° during computation~~, with the excess boundary removed~~ . The excluded margins are clipped after processing~~to ensure accuracy in~~ , leaving the ~~core~~ retained region for accurate results.

significantly improves the model's precision, particularly at sub-region boundaries. ~~Addressing edge effects significantly enhances the precision of the VGGA modelby ensuring that derivative calculations at boundaries are reliable.~~

3.2 Model building

~~The vertical gradient of gravity (VGG) is composed~~

The VGG consists of two components: the vertical gradient of normal gravity and the ~~vertical gradient of gravity anomaly (VGGA). The VGGA was initially derived using~~ VGGA. In this study, the VGGA was derived from the MSS model. Since the vertical gradient of normal gravity is a ~~function of latitude~~latitude-dependent function, the VGGA alone ~~is sufficient to reveal the~~ suffices to reveal Earth's internal structure. Therefore, only the VGGA was ~~calculated in this study, without incorporating~~ computed in this research, excluding the vertical gradient of normal gravity.

The VGGA represents the difference between the gradient of actual gravity and ~~the~~ normal gravity, ~~highlighting~~ emphasizing deviations caused by factors such as uneven mass distribution~~within the Earth~~, topographical variations, and subsurface structures. These deviations provide valuable insights into ~~subsurface~~ geological formations and geophysical characteristics ~~. By combining gravity anomalies with VGGA, a more detailed and comprehensive representation of the ocean gravity field can be achieved~~beneath the Earth's surface.

Assuming the disturbing potential, denoted as T, at a point on the geoid, the gravity anomaly is computed using the fundamental equations of physical geodesy (Moritz, 1980; Hofmann-Wellenhof and Moritz, 2006):

$$\Delta g = -\frac{\partial T}{\partial h} + \frac{1}{\gamma}\frac{\partial \gamma}{\partial h} T \tag{1}$$

where ~~,~~ Δg ~~represents~~ denotes the gravity anomaly, ~~and~~ γ is the normal gravity at the point~~. If the ellipsoidis approximated as a sphere~~, and h is the orthometric height. For a spherical approximation of the ellipsoid, the following ~~approximation~~ relationship

holds:

$$\frac{\partial}{\partial h} \cong \frac{\partial}{\partial r} \tag{2}$$

According to Bruns' formula, γ can be replaced by G, ~~resulting in~~ leading to the following relationship outside the Earth:

$$\Delta g = -\frac{\partial T}{\partial r} - \frac{2}{r}T \tag{3}$$

By differentiating ~~the above equation and using~~ Equation (3) and applying Laplace's equation ~~, a~~ ($\nabla^2 U = 0$), the vertical derivative of the gravity anomaly can be expressed in terms of its horizontal derivatives. This results in the following formula for calculating the VGGA, ~~involving~~ which incorporates the geoid as well as its first and second horizontal derivatives~~, can be derived~~:

$$\frac{\partial \Delta g}{\partial r} = \frac{2G}{R^2}N - \frac{G}{R^2}\tan\varphi\frac{\partial N}{\partial \varphi} + \frac{G}{R^2}\frac{\partial^2 N}{\partial \varphi^2} + \frac{G}{R^2\cos^2\varphi}\frac{\partial^2 N}{\partial \lambda^2} \tag{4}$$

where N represents the geoid height, G ~~represents~~ is the mean gravity~~value, and~~ , φ ~~represents~~ is the geographic latitude~~of the calculation point.~~ , and λ is the geographic longitude.

This equation demonstrates how the VGGA is a direct function of the geoid height N, as well as its first and second derivatives in the latitude (φ) and longitude (λ) directions. The coupling of horizontal and vertical derivatives is a direct consequence of Laplace's equation, ensuring that the short-wavelength components in the vertical direction are determined entirely by the horizontal variations of the geoid.

After establishing the regional partitioning strategy and deriving the method for calculating the VGGA, the ~~mean dynamic topography (MDT) model from CNES-CLS22~~ CNES-CLS22 MDT model was interpolated onto the DTU21 MSS grid using cubic spline interpolation to increase the resolution. This increased the resolution to $1' \times 1'$ and ensured consistency between the two datasets. The choice of cubic spline interpolation was based on its superior ability to provide smooth and continuous estimates, which is essential for accurately capturing the fine-scale geoid variations. This interpolation step enhances the spatial detail of the MDT, facilitating more precise geoid extraction. Subsequently, the interpolated MDT model was subtracted from the DTU21 MSS model to obtain the geoid, denoted by N:

$$N = MSS - MDT_{\text{inter}} \tag{5}$$

Next, the remove-restore method was ~~used~~ employed to isolate the ~~residual geoid signal~~ short-wavelength residual geoid by subtracting the long-wavelength component, represented by the XGM2019e_2190 geoid, from the ~~original~~ full-wavelength geoid. This ~~step separates the long-wavelength~~ process separates the geoid into its long- and short-wavelength components~~of the geoid~~. By removing the long-wavelength signals, the short-wavelength residual geoid ~~remains, highlighting~~ highlights local variations and finer details in the geoid ~~structure (Hwang, 1999).~~ (Hwang, 1999):

$$N_{\text{res}} = N - N_{\text{ref}} \tag{6}$$

where N_{res} denotes the short-wavelength residual geoid, N represents the full-wavelength geoid, and N_{ref} represents the long-wavelength component derived from the XGM2019e_2190 geoid. Through the remove-restore method, the gridded MSS

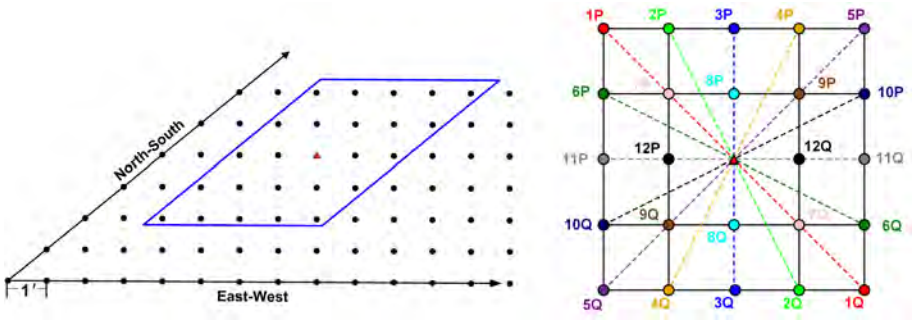

Figure 3. Illustration of the north-south and east-west components of the derivative of the residual geoid based on multidirectional MSS data, using a $5' \times 5'$ window as an example. The red triangle represents the center point for calculation, and P-Q pairs indicate 12 possible combinations used for ~~multi-directional~~ multidirectional gradient computation.

~~provided a gridded form of~~ data were used to derive the residual geoid, N_{res}. The long-wavelength signals, primarily influenced by the Earth's geopotential field, were removed from the MSS using a reference geoid model, leaving the residual geoid that captures shorter-wavelength features associated with local oceanographic and topographic variations. For each calculation point, the second-order derivatives of N_{res} were computed in multiple directions using a weighted least squares method. ~~The~~ This approach allowed for the extraction of detailed gravity field information by calculating the second-order partial derivatives in the north-south and east-west components~~were then computed to optimize the extraction of gravity field information, ensuring accuracy and reliability. This approach takes into account the~~ . The weighted least squares method ensured that the calculations accounted for the complexity of ocean topography~~to enhance gravity field information extraction, ensuring both~~ , enhancing the accuracy and reliability of the derived gravity field information. The following ~~formula is used for calculation:~~ equation was used for the calculation:

$$\frac{\partial^2 N_{\text{res},(kP,kQ)}}{\partial l^2} = \frac{\partial^2 N_{\text{res},(kP,kQ)}}{\partial \varphi^2} \cos^2 a_{kP,kQ} + 2\frac{\partial^2 N_{\text{res},(kP,kQ)}}{\partial \varphi \partial \lambda} \sin a_{kP,kQ} \cos a_{kP,kQ} + \frac{\partial^2 N_{\text{res},(kP,kQ)}}{\partial \lambda^2} \sin^2 a_{kP,kQ} \tag{7}$$

where k represents the number of equations, ~~and~~ α ~~represents~~ is the geodetic azimuth between points P and Q~~. According to the method in (Zhou et al., 2023), a~~ , and l denotes the horizontal distance between these two points. A calculation window size of $17' \times 17'$ was determined. For a given calculation window size of ~~$i' \times i'$~~ $i' \times i'$, the number of equations is calculated as ~~:~~ $k = (i^2 - 1)/2$. For example, when ~~$i = 5$~~ $i = 5$, 12 sets of second-order derivatives of N_{res} are obtained, resulting in 12 equations.

Figure 3 illustrates the calculation process using a $5' \times 5'$ calculation window. In the actual computations, a larger $17' \times 17'$ window was ~~used~~employed to ensure sufficient coverage and improve the accuracy of the gradient extraction.

The matrix form of Equation 7 can be represented as:

$$\mathbf{V} = \mathbf{AX} - \mathbf{L} \tag{8}$$

where $\mathbf{V}$ represents the residual vector, and $\mathbf{A}$ ~~represents~~ denotes the coefficient matrix composed of the north-south and east-west second-order partial derivatives:

$$\mathbf{A} = \begin{pmatrix} \cos^2\alpha_{1P,1Q} & 2\sin\alpha_{1P,1Q}\cos\alpha_{1P,1Q} & \sin^2\alpha_{1P,1Q} \\ \cos^2\alpha_{2P,2Q} & 2\sin\alpha_{2P,2Q}\cos\alpha_{2P,2Q} & \sin^2\alpha_{2P,2Q} \\ \cos^2\alpha_{3P,3Q} & 2\sin\alpha_{3P,3Q}\cos\alpha_{3P,3Q} & \sin^2\alpha_{3P,3Q} \\ \vdots & \vdots & \vdots \\ \cos^2\alpha_{(k-1)P,(k-1)Q} & 2\sin\alpha_{(k-1)P,(k-1)Q}\cos\alpha_{(k-1)P,(k-1)Q} & \sin^2\alpha_{(k-1)P,(k-1)Q} \\ \cos^2\alpha_{kP,kQ} & 2\sin\alpha_{kP,kQ}\cos\alpha_{kP,kQ} & \sin^2\alpha_{kP,kQ} \end{pmatrix} \tag{9}$$

$\mathbf{X}$ ~~consists of two vectors representing~~ is a vector containing the second-order partial derivatives of the residual geoid in the north-south and east-west ~~directions~~components. Once the residual vector ~~and coefficient matrix~~ $\mathbf{V}$ and the coefficient matrix $\mathbf{A}$ are established, the ~~next step involves applying the weighting matrix~~ weighting matrix is applied to balance data contributions from different directions. The solution for $\mathbf{X}$, corresponding to the ~~north-south and east-west components of the~~ second-order partial derivatives of the residual geoid, is determined by minimizing the cost function ~~: $\Psi = V^T W V$:~~ $\Psi = \mathbf{V}^T\mathbf{W}\mathbf{V}$. The solution is given by:

$$\mathbf{X} = (\mathbf{A}^T\mathbf{W}\mathbf{A})^{-1}(\mathbf{A}\mathbf{W}\mathbf{V}) \tag{10}$$

where W is the weighting matrix, calculated using an inverse distance formula: $W = 1/l^2$. This formula gives higher weights to closer points, thereby balancing data contributions and ensuring accuracy and reliability in the results.

~~Unlike this~~ After computing the residual VGGAs, they were combined with the long-wavelength component of the VGGA from the XGM2019e_2190 model as part of the remove-restore process. This step was crucial to mitigate the influence of long-wavelength signals, which could distort the calculation of finer, short-wavelength variations in the geoid. As a result, the resulting VGGA models accurately captured short-wavelength geoid variations, while effectively excluding long-wavelength signals.

To address boundary effects, the edges of each subregion were initially expanded. This expansion was necessary to suppress edge artifacts during calculations. Subsequently, the expanded regions were clipped to remove overlaps, ensuring that only the valid central area of each subregion was retained. Once this step was completed, the VGGA models for each subregion were prepared for comparison with existing models and for merging into a continuous global model.

In contrast to this study, which calculates the VGGA by deriving the second-order horizontal partial derivatives of the geoid, the VGGA model in ~~the~~ SIO V32.1 ~~dataset is computed from~~ curv is computed using the first-order derivatives of the DOV's north-south and east-west components (Muhammad et al., 2010; Sandwell and Smith, 1997, 2009). ~~By contrast, the VGGA model relies on first-order derivative calculations.~~ To evaluate and validate the accuracy of the proposed method, the VGGA model constructed in this study was compared with the SIO V32.1 ~~dataset~~curv.

Following the computation and validation of each subregion, these subregions were merged to construct a continuous marine VGGA model spanning from 80° S to 80° N, designated as SDUST2023VGGA.

The workflow of the study is illustrated in Figure 4.

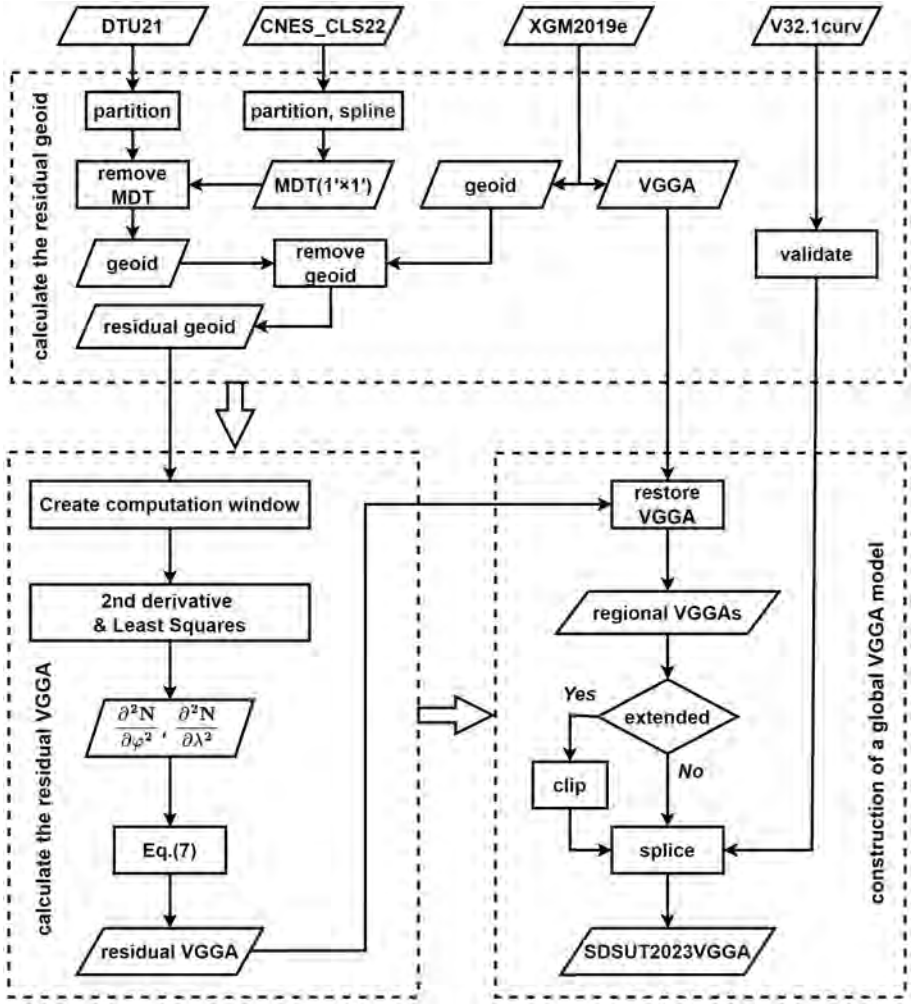

Figure 4. Workflow for constructing the VGGA model using the DTU21 MSS, CNES-CLS22 MDT and XGM2019e~~.~~ 2190.

4 Results and analysis

After establishing the regional partitioning strategy, the DTU21 MSS was ~~used~~utilized, and the CNES-CLS22 MDT was subtracted to derive the geoid ~~. Subsequently, the~~ height. The XGM2019e~~gravity field was~~ 2190 gravity field model was subsequently subtracted to obtain the residual geoid. A ~~multi-directional method~~ multidirectional approach was applied to the ~~MSS~~ geoid height data to calculate the second-order partial derivatives, and the VGGA ~~)~~ for each sub-region was ~~estimated through the~~ derived using the weighted least squares method. ~~The~~ These sub-regional VGGA models were ~~then combined~~ integrated to construct a global VGGA model for oceanic regions.

Due to the limited availability of direct global VGGA observations, the satellite altimetry-based SIO V32.1 curv model served as a reference for comparison. The inversion statistics for each sub-region are presented in Table 1 presents the inversion

Table 1. Statistical RMS differences obtained by subtracting the constructed ~~VGGA models~~ SDUST2023VGGA model from the SIO V32.1 curv model (unit: E)

	B1	B2	B3	B4	B5	B6
L1	10.03	4.55	5.67	5.60	6.12	9.91
L2	11.44	5.06	6.03	4.24	7.88	11.82
L3	10.24	5.43	5.65	6.82	17.99	18.76
L4	14.92	8.97	8.58	11.69	9.13	16.92
L5	20.64	5.45	6.24	5.43	6.14	14.39
L6	12.88	5.96	4.76	6.54	7.10	12.63
L7	11.98	5.76	7.02	9.38	12.59	10.41
L8	13.10	5.94	8.49	10.35	68.39	6.83
L9	11.55	5.78	6.02	6.90	64.41	7.72
L10	16.63	5.26	7.12	10.35	38.25	11.08
L11	14.43	5.62	14.62	9.63	9.98	9.33
L12	17.00	6.66	8.74	6.04	6.35	8.71

statistics for each sub-region, highlighting discrepancies between the curv and SDUST2023VGGA models. The differences between the two models were analyzed to assess and validate the accuracy of the computational method used in this study.

~~Table 1 presents a statistical assessment of the root mean square (RMS) differences between the constructed VGGA models and the SIO V32.1 curv model for each sub-region.~~

The analysis of the ~~longitudinal direction~~ RMS differences in Table 1 reveals significant variability along both longitudinal (L1 to L12) ~~shows significant fluctuations without a clear trend~~ and latitudinal (B1 to B6) directions. Longitudinally, no clear trend is observed, indicating that ~~longitudinal VGGAs are affected by various~~ VGGA discrepancies are influenced by diverse geographical and geophysical factors, such as ~~variations in~~ seafloor topography and local tectonics. In the latitudinal direction~~(B1 to B6), particularly in the~~ , lower RMS values are evident in equatorial regions (B3 and B4), ~~lower anomaly values were observed, likely due to the high quality of altimetry datain these areas~~which likely benefit from high-quality satellite altimetry data. Conversely, sub-region B6 exhibits higher RMS values~~were noted in sub-region B6, especially~~ , particularly in L3, L4, and L5, ~~indicating the influence of more~~ reflecting the complex bathymetric features and tectonic activity ~~typical~~ characteristic of sub-polar regions.

Further analysis, ~~along~~ in conjunction with the ocean depth model ~~in Figure 1~~(Figure 1), suggests that significant ~~VGGAs~~ VGGA variations near the equator are linked to deep ocean trenches, mid-ocean ridges, and other major geological structures that ~~notably affect~~ strongly influence the Earth's mass distribution. ~~Additionally, longitudinal~~ Longitudinally, sub-regions such as L1, L2, and L6 generally exhibit lower RMS differences across most latitude bands, ~~indicating potentially~~ suggesting more homogeneous geoid characteristics in these ~~longitudinal strips~~regions.

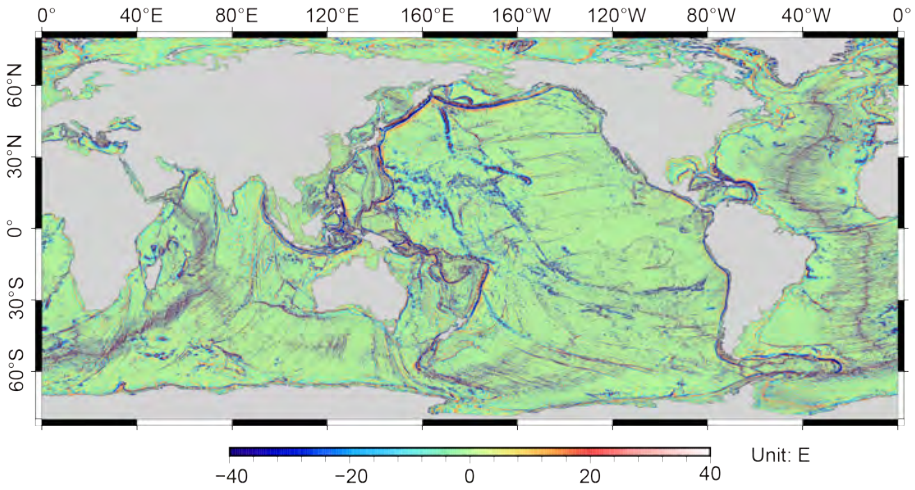

Figure 5. Global VGGA model ~~SDUST2023VGGA~~ SDUSTVGGA constructed from the DTU21 MSS~~data~~.

Upon completing the model construction for all sub-regions, the excess portions were trimmed to ~~create the~~ produce a continuous global VGGA model for oceanic regions, ~~named~~ designated as SDUST2023VGGA ~~. The~~ (hereafter referred to as SDUSTVGGA). The final model spans longitudes from 0° to 360° and latitudes from 80° S to 80° N~~, as illustrated in Figure 5~~. Figure 5 illustrates the resulting global VGGA model.

Investigating Earth's tectonic activities and their impact on gravitational fields enhances our understanding of geophysical dynamics. Supported by the visualizations in Figure 5, this study examines key tectonic features, including mid-ocean ridges, abyssal plains, subduction zones, and volcanically active ~~zones. These elements are pivotal~~ regions. These features play pivotal roles in shaping Earth's landscape and influencing the observed patterns of VGGAs. The discussions that follow will analyze how these features contribute to gravity field variations and their implications for understanding underlying geodynamic processes.

Mid-ocean ridges~~serve as prominent features~~, representing divergent boundaries in the global plate tectonic system, are prominent features. Notable examples include the Mid-Atlantic Ridge and the East Pacific Rise, both ~~of which are~~ characterized by mantle upwelling, where magma rises and solidifies to form new oceanic crust~~(?)~~. This process results in localized density reduction~~. This creates~~, creating a stark contrast with the surrounding older, cooler oceanic crust ~~,~~ and leading to pronounced ~~variations in the gravity field (Álvarez et al., 2018). Mantle upwelling influences the VGGA along mid-ocean ridges by reducing density, reflecting crustal expansion and the formation of new oceanic material.~~

gravity field variations (Álvarez et al., 2018; Michael and Cornell, 1998; Escartín et al., 2008). For instance, the Mid-Atlantic Ridge~~extends southward from Iceland~~, extending from Iceland (65° N, 18° W~~, passes through the North Atlantic 45° N, 30° W, and reaches the South Atlantic~~) to the South Atlantic (40° S, 10° W~~(Rao et al., 2004). On the gradient map, this ridge~~), appears as a linear high-gradient region on the gradient map, reflecting crustal changes due to mantle upwelling and expansion (Rao et al., 2004). Similarly, the East Pacific Rise, ~~a volcanically active chain~~ located in the eastern Pacific ~~, now extends~~ and

trending southwestward from 55° S, 130° W~~and trends southwestward. This ridge ~~, is characterized by significant volcanic activity ~~, and~~ hydrothermal vents, ~~and mantle upwelling,~~ contributing to crustal expansion ~~in this area (Yu et al., 2022). The Central Pacific Region, extending from 10° N to 30° N and 140° W to 170° W, also features significant volcanic activity and crustal thickness variations due to ongoing volcanic and tectonic processes (Rao et al., 2004). This region's gravity anomalies are influenced by the uplift of the Hawaiian volcanic chain, exemplifying the complex interplay of tectonic and volcanic dynamics (?).~~ and VGGAs (Yu et al., 2022).

Deep-sea plains, typically linked to plate subsidence, where the oceanic crust gradually sinks under its weight, result in relatively stable gradient~~(?)~~. The Pacific Abyssal Plain, extending from approximately 30° N to 60° S and spanning longitudes from 150° W to 150° E, is characterized by a relatively thin crust and smooth, low-gradient regions on the map. This uniformity is influenced by low-density, fine-grained sediments, such as silt and clay, that cover the plain, minimizing variations in crustal density ~~(?)~~(Smith and Sandwell, 1997; Clift and Vannucchi, 2004). Similarly, the Atlantic Abyssal Plains, primarily distributed between 40° N and 60° S and from 30° W to 30° E, display low ~~gradient of gravity anomaly~~ VGGA due to similar sedimentary characteristics, which dampen tectonic activity and stabilize the crust. The Indian Ocean Abyssal Plains, located between 30° S and 60° S and spanning longitudes from 60° E to 100° E, exhibit comparable low-gradients, highlighting the effects of thick, fine-grained sediment deposits in maintaining crustal stability. ~~These examples illustrate the global distribution of abyssal plains as tectonically stable regions, with low-density sediments contributing to their distinct gradient of gravity anomaly patterns.~~

Subduction zones~~are regions where tectonic processes cause ~~, where one tectonic plate is forced beneath another, are areas of dramatic changes in crustal density ~~, leading to ~~that generate distinct low VGGAs. For instance, the Mariana Trench, located at 11° N, 142° E, is the world's deepest oceanic trench, with the Challenger Deep reaching a depth of 10,994 meters. ~~At these depths , the pressure ~~The extreme pressure at these depths increases water density by nearly 5%, ~~contributing to significant~~ significantly influencing gravity field variations~~,~~. These effects are represented as dark blue areas on Figure 5, indicating low VGGAs ~~(?)~~(Han et al., 2018). Similarly, the Peru-Chile Trench, situated at approximately 23° S, 71° W, marks the subduction of the Nazca Plate beneath the South American Plate~~, which ~~. This tectonic process generates significant seismic and volcanic activity, contributing to notable low VGGAs ~~(Álvarez et al., 2018; ?)~~in the region (Álvarez et al., 2018).

Volcanically active zones~~exhibit notable VGGAs caused ~~, characterized by crustal uplift, fractures, and magma activity~~. These regions often ~~, show localized high ~~gradient of gravity anomaly due to ~~VGGAs due to the presence of magma chambers and fault zones. For ~~instance~~example, the Hawaiian Volcanic Chain, ~~which spans from approximately ~~spanning from 18° N ~~to29~~to 29° N and 155° W to 172° W, is a hotspot-driven volcanic chain with notable ~~gravity anomalies ~~VGGAs caused by magma upwelling (Poland and Carbone, 2016). Similarly, the Galápagos Volcanic Chain, located from 0° N, 89° W to 1° N, 92° W, experiences significant volcanic activity ~~due to ~~driven by the Galápagos hotspot, with localized density variations contributing to ~~localized high gravity anomalies ~~high VGGAs (Vigouroux et al., 2008). The New Zealand Volcanic Arc, ~~located ~~situated at the convergence of the Pacific and Indo-Australian Plates (35° S to 39° S, 175° E to 179° E), ~~shows similar high-gradient~~ displays similar high gradients associated with subsurface magma activity and crustal thickness variations. These ~~volcanic zones, especially in regions like the Central Pacific Region, illustrate the complex interactions between tectonic activity and mantle processes~~regions exemplify how volcanic and tectonic dynamics interact to shape localized gravity anomaly patterns.

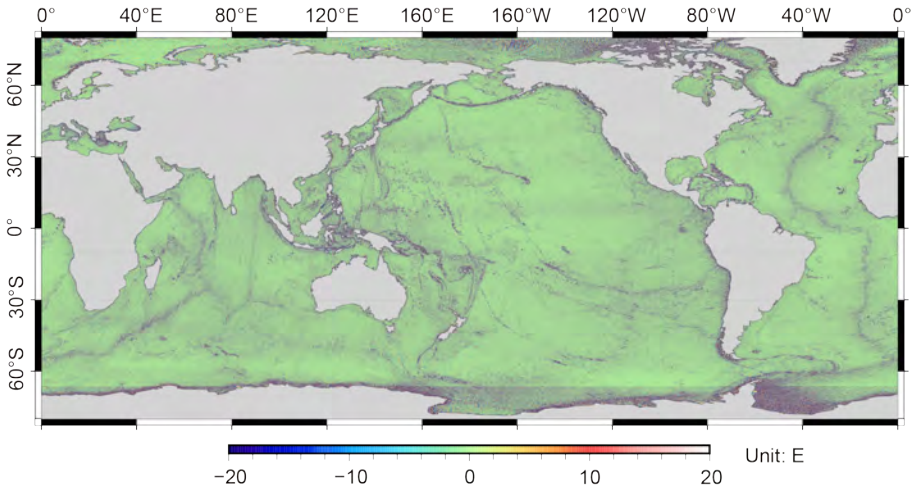

Figure 6. The spatial distribution of differences obtained by subtracting the ~~constructed VGGA~~ SDUSTVGGA model from the SIO V32.1 curv model

The ~~VGGA~~ SDUSTVGGA map reveals crucial density variations within the crust and mantle, providing an indispensable tool for identifying geological structures, exploring mineral resources, and assessing seismic and volcanic risks. The findings from this analysis emphasize the utility of VGGAs in elucidating tectonic and volcanic processes on a global scale.

Given the challenges in obtaining direct VGGA measurements, the reliability of the ~~VGGA~~ SDUSTVGGA model was assessed by comparison with the SIO V32.1 curv model. The ~~difference between the VGGA~~ differences between the SDUSTVGGA model and the SIO V32.1 curv model produced a residual model, illustrated in Figure 6. The SIO V32.1 curv model, based on satellite altimetry data, serves as ~~an effective~~ a robust reference for cross-validation.

Figure 6 presents the global spatial distribution of differences between the ~~VGGA~~ SDUSTVGGA model and the SIO V32.1 curv model. In most regions, the two models demonstrate strong consistency, exhibiting generally low residuals across the oceans. This consistency is particularly evident in mid and low latitudes, where satellite altimetry data tends to be more accurate and less affected by atmospheric or sea-ice interference.

Furthermore, increased differences between the models are evident from 66° S to 80° S, with a distinct seam appearing at 66° S. This seam likely arises from differences in data quality and processing methods applied to polar regions, underscoring the challenges in these areas. ~~These challenges arise from factors such as limited satellite coverage, interference from sea ice, and the need for distinct data calibration approaches in high-latitude zones. Such systematic variations in preprocessing may contribute to the observed discrepancies.~~

To mitigate the impact of outliers and better assess data quality, a two-step filtering process was applied ~~in the analysis of~~ independently to the original data during the analysis of residual differences between the two models. Here, ~~σ~~ σ represents the standard deviation (STD), measuring the dispersion of data points from the mean. First, a tenfold STD (~~10σ~~10σ) filter was applied to the original data to exclude extreme outliers, which removed 0.07% of the data~~, reducing extreme outliers.~~

Table 2. Statistical differences obtained by subtracting the ~~constructed VGGA~~ SDUSTVGGA model from the SIO V32.1 curv model (unit: E)

~~Data~~ Filter Type	Max	Min	Mean	STD	RMS	Exclusion Rate
~~difference~~ Raw	791.01	-673.00	-0.08	7.24	8.50	-
10σ ~~filter~~ Filter	72.31	-72.47	-0.09	6.39	7.61	0.07%
3σ ~~filter~~ Filter	21.64	-21.79	-0.07	4.82	5.85	1.41%

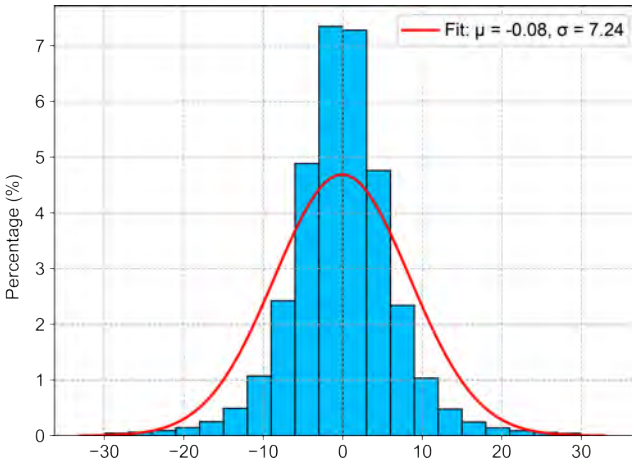

Figure 7. The histogram of differences obtained by subtracting the ~~constructed VGGA~~ SDUSTVGGA model from the SIO V32.1 curv model, with fit parameters: μ representing the mean and σ representing the STD

~~Then~~. Following this, a stricter threefold STD (~~3σ~~3σ) filter was applied, ~~which removed an additional 1.41% of the~~ again to the original data, targeting moderate outliers and removing 1.41% of the data. This hierarchical filtering approach refined the residuals by excluding outliers, facilitating a more detailed and accurate analysis of the model's accuracy and robustness. The statistical information and histogram of the residual differences are presented in Table 2 and Figure 7, respectively.

Globally, the ~~VGGA~~ SDUSTVGGA model derived from ~~multi-directional~~ multidirectional MSS data shows strong consistency with the SIO V32.1 curv model. Initial statistical analysis of the model differences revealed a maximum of 791.01 E and a minimum of -673.00 E, with a mean of -0.08 E, indicating an approximately symmetric distribution centered around zero. The STD was 7.24 E, and the ~~root mean square (RMS) error~~ RMS was 8.50 E, suggesting the presence of outliers, potentially resulting from satellite altimetry limitations in coastal areas and regions with complex seafloor topography.

To assess the impact of outliers on the statistical metrics, data points deviating by more than $\pm$10 and $\pm$3 times the STD from the mean were progressively removed, followed by a re-analysis of the remaining dataset. After excluding data points exceeding $\pm$10 times the STD, the maximum and minimum values were reduced to 72.31 E and -72.47 E, respectively, while the mean remained at -0.09 E. This indicates that extreme outliers significantly impacted the STD and RMS error; however, since these outliers represented only 0.07% of the total data, their effect on the mean was minimal.

Further exclusion of data points deviating by more than ±3 times the STD (1.41% of the data) reduced the maximum and minimum values to 21.64 E and -21.79 E, with the mean shifting slightly to -0.07 E. This demonstrates that removing more outliers led to a continued decrease in the STD and RMS error, indicating reduced data dispersion and an improved fit. Nevertheless, the stability of the mean suggests that the core results were robust despite the presence of outliers. This stability implies that the underlying model retains its predictive capacity and reliability, even when outliers are present, which is crucial for ensuring the robustness of the ~~VGGA~~ SDUSTVGGA model in diverse oceanic regions.

5 Discussion

5.1 Validation and analysis of model performance

Coastlines and islands can contaminate altimetry waveform data (Guo et al., 2010), which significantly affects the accuracy of altimetry measurements and, consequently, the inversion results of gradients of grvity anomaly. In deep-sea regions, complex ocean dynamics such as deep currents, internal waves, and eddies substantially impact sea surface morphology by causing undulations and localized changes in sea surface height (Khaki et al., 2015). Additionally, the satellite's orbital inclination affects its coverage of different latitudinal regions, potentially resulting in higher data quality at mid-latitudes and reduced coverage at the poles (Sandwell et al., 2006), thus influencing the quality of altimetry data. Furthermore, the slope of the seafloor topography plays a crucial role in the accuracy of altimetry data (Sandwell and Smith, 2014). Steeper slopes increase the complexity of sea surface morphology, resulting in more irregular altimetry waveforms and reduced data precision. Larger seafloor slopes increase the complexity of sea surface morphology, resulting in irregular signals in the altimetry waveforms. This reduces the precision of the data, thus affecting the reliability of the models constructed from these measurements. ~~Coastlines and islands can contaminate altimetry waveform data (Guo et al., 2010), which significantly affects the accuracy of altimetry measurements and, consequently, the inversion results of gradients of gravity anomaly. In deep-sea regions, complex ocean dynamics such as deep currents, internal waves, and eddies substantially impact sea surface morphology by causing undulations and localized changes in sea surface height (Khaki et al., 2015). Additionally, the satellite's orbital inclination affects its coverage of different latitudinal regions, potentially resulting in higher data quality at mid-latitudes and reduced coverage at the poles (Sandwell et al., 2006), thus influencing the quality of altimetry data. Furthermore, the slope of the seafloor topography plays a crucial role in the accuracy of altimetry data (Sandwell and Smith, 2014). Steeper slopes increase the complexity of sea surface morphology, resulting in more irregular altimetry waveforms and reduced data precision. Larger seafloor slopes increase the complexity of sea surface morphology, resulting in irregular signals in the altimetry waveforms. This reduces the precision of the data, thus affecting the reliability of the models constructed from these measurements.~~

To evaluate the impact of ~~these~~ various factors on the inversion results, ~~this study uses~~ the residual model obtained in Sect. ~~4,~~ 4 was used. This model was calculated by subtracting the ~~VGGA~~ SDUSTVGGA model from the SIO V32.1 curv model. The ~~residuals are categorized into several~~ analysis was conducted using the data without σ-based filtering to ensure that all data points, including potential outliers, were considered. The residuals were categorized into intervals based on offshore distance,

Table 3. Statistical summary of differences obtained by subtracting the ~~VGGA~~ SDUSTVGGA model from SIO V32.1 curv at different offshore distances (unit: E)

Offshore Distance (km)	Max	Min	Mean	STD	RMS
$[0, 50)$	791.01	-673.00	-0.81	18.37	18.39
$[50, 100)$	247.45	-163.67	-0.08	7.55	7.55
$[100, 150)$	187.57	-119.80	-0.05	6.54	6.54
$[150, 200)$	151.67	-102.02	-0.05	6.21	6.21
$[200, 250)$	133.24	-88.72	-0.04	6.04	6.04
$[250, 300)$	130.08	-129.01	-0.03	5.88	5.88
$[300, \infty)$	249.47	-149.96	-0.03	5.29	5.29

Table 4. Statistical summary of differences obtained by subtracting the ~~VGGA~~ SDUSTVGGA model from SIO V32.1 curv at different ocean depths (unit: E)

Depth (km)	Max	Min	Mean	STD	RMS
$[0, 1)$	791.01	-671.45	-0.20	13.39	13.39
$[1, 2)$	709.38	-442.57	-0.01	10.05	10.05
$[2, 3)$	315.07	-492.87	0.07	7.79	7.79
$[3, 4)$	262.21	-557.07	-0.07	6.03	6.03
$[4, 5)$	134.04	-162.81	-0.11	4.83	4.83
$[5, \infty)$	42.69	-93.17	-0.16	4.21	4.22

sea depth, latitude, and seafloor topography slope to examine ~~the influence of these factors on~~ how these factors influenced the model construction results. The findings of this analysis are presented in Tables 3 through 6 and Figure 8.

Table 3 illustrates the impact of offshore distance on the inversion results. As the distance from the coastline increases, the STD of the residual model consistently decreases. Notably, beyond 50 kilometers from the coastline, the reduction in the STD becomes less pronounced. This is likely due to the reduced impact of shallow waters on satellite echo waveforms, which results in less pronounced improvements in data accuracy. In summary, regions closer to the coastline are associated with larger ~~residual values~~residuals, while deep-sea regions farther from the coast exhibit lower ~~residual values~~residuals.

Table 4 provides statistical data of residuals across different sea depth intervals. In shallow waters (0-1 km), the residuals show considerable fluctuation, including extreme maximum and minimum values, as well as higher STD and RMS errors. These fluctuations may result from rapid seafloor topography changes in shallow regions, which substantially impact the ~~vertical gradient of gravity anomaly~~ VGGA calculations. As depth increases, the ~~residual values~~ residuals gradually become smaller and more concentrated, indicating that the model performs more stably and reliably in deep-water areas. This stability can be attributed to the relatively smooth seafloor topography in deeper waters, which introduces fewer interference factors. These results validate that the DTU21 MSS model not only effectively handles oceanic phenomena, such as eddies,

Table 5. Statistical summary of differences obtained by subtracting the ~~VGGA~~ SDUSTVGGA model from SIO V32.1 curv at different latitudes (unit: E)

Latitude (°)	Max	Min	Mean	STD	RMS
$[-60,-50)$	670.36	-339.30	-0.02	5.73	5.73
$[-50,-40)$	791.01	-673.00	-0.04	5.91	5.91
$[-40,-30)$	262.57	-193.64	-0.05	5.96	5.96
$[-30,-20)$	267.98	-257.79	-0.05	6.25	6.25
$[-20,-10)$	258.93	-259.24	-0.07	6.72	6.72
$[-10,0)$	397.26	-650.42	-0.15	8.11	8.11
$[0,10)$	463.47	-415.12	-0.09	7.44	7.44
$[10,20)$	479.81	-557.07	-0.15	7.46	7.46
$[20,30)$	351.52	-554.68	-0.11	7.60	7.60
$[30,40)$	353.69	-529.66	-0.20	7.37	7.38
$[40,50)$	425.17	-255.52	-0.21	7.31	7.31
$[50,60)$	668.93	-504.54	-0.17	8.78	8.78
$[60,70)$	677.85	-409.98	-0.19	12.43	12.44
$[70,80]$	428.13	-219.00	-0.05	11.40	11.41

Table 6. Statistical summary of differences obtained by subtracting the ~~VGGA~~ SDUSTVGGA model from SIO V32.1 curv at different seafloor slopes (unit: E)

Slope (%)	Max	Min	Mean	STD	RMS
$[0,1)$	682.50	-641.65	-0.17	7.18	7.19
$[1,2)$	668.85	-671.45	-0.10	6.47	6.47
$[2,3)$	740.85	-673.00	-0.07	6.65	6.66
$[3,4)$	754.55	-650.42	-0.07	7.06	7.06
$[4,5)$	668.93	-446.56	-0.06	7.50	7.50
$[5,6)$	764.00	-464.99	-0.04	7.93	7.93
$[6,7)$	758.45	-509.98	-0.02	8.36	8.36
$[7,8)$	638.45	-412.81	0.01	8.73	8.73
$[8,9)$	791.01	-366.35	0.02	9.11	9.11
$[9,10)$	768.50	-521.05	0.03	9.60	9.60
$[10,\infty)$	768.05	-557.07	0.05	12.32	12.32

but also demonstrates a high level of completeness and robustness in capturing sea surface variability across different ocean environments.

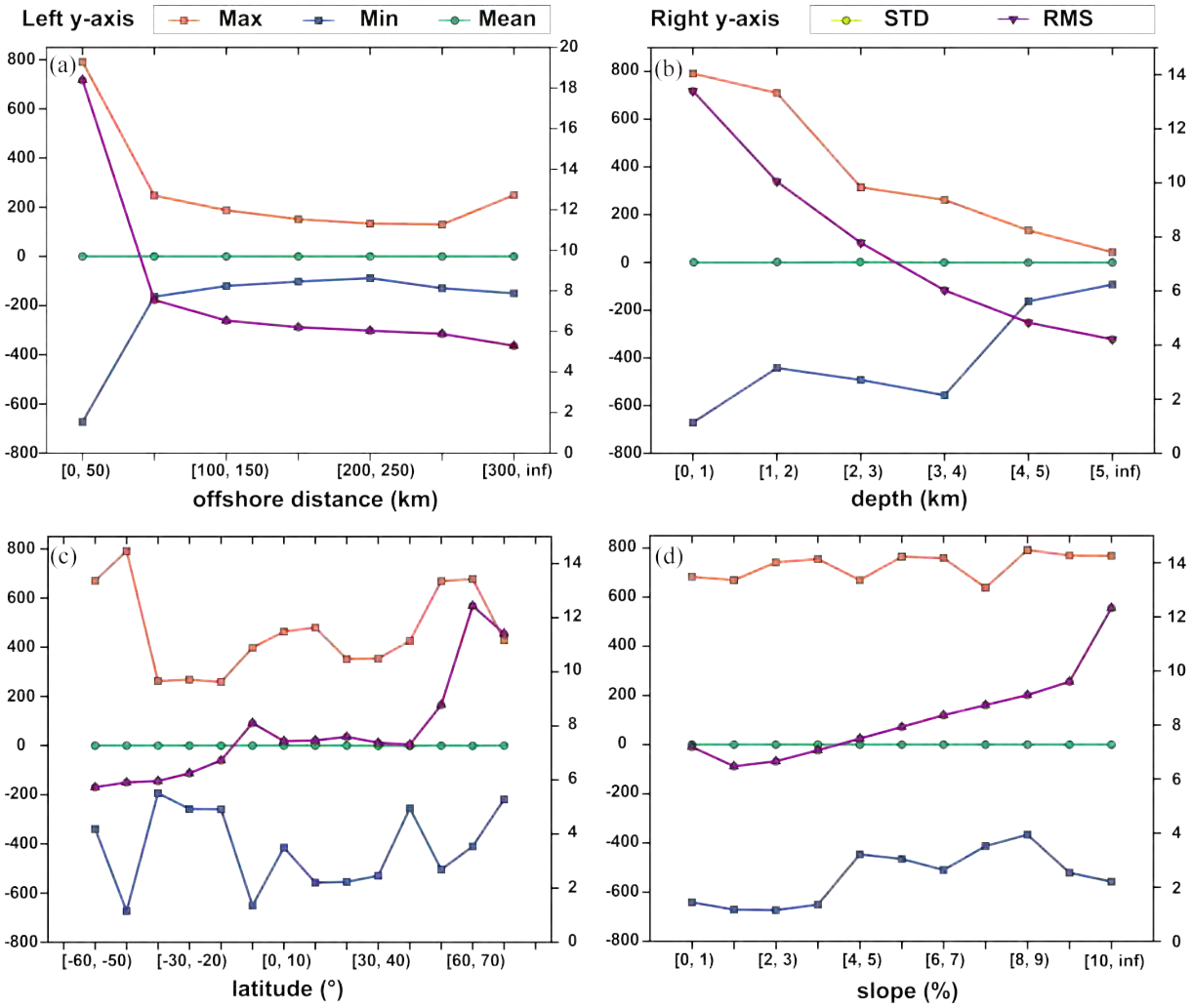

Figure 8. Residuals obtained by subtracting the ~~constructed VGGA~~ SDUSTVGGA model from the SIO V32.1 curv model, categorized by: (a) offshore distance (km), (b) seafloor slope (%), (c) sea depth (m), and (d) latitude (°). The left y-axis represents the max, min, and mean residuals (unit: E), while the right y-axis represents the STD and RMS of the residuals (unit: E). Note: STD and RMS curves overlap, appearing as a single line.

The analysis of Table 5 shows that in the latitude intervals of [-60, -50)°, [-50, -40)°, [-10, 0)°, [60, 70)°, and [70, 80]°, the model exhibits larger extreme values, with maxima reaching 670.36 E, 791.01 E, 397.26 E, 677.85 E, and 428.13 E, respectively. These high values indicate significant inconsistencies between models in these regions, especially in the high-latitude intervals such as [60, 70)° and [70, 80)°. The STD and RMS values are significantly higher in these intervals, at 12.43 E and 11.40 E, respectively, further confirming the greater inconsistencies in high-latitude regions. In contrast, mid- and low-latitude regions exhibit smaller extreme value ranges and lower RMS values, indicating greater model consistency. These results

Table 7. Statistical comparison of differences obtained by subtracting the ~~VGGA~~ SDUSTVGGA model from the SIO V32.1 curv model in different regions (unit: E)

Regions	Lat and lon	Mean Depth (m)	Max	Min	Mean	STD	RMS
A	$-5^\circ \sim 5^\circ, -120^\circ \sim -110^\circ$	-4077.64	25.64	-22.27	-0.05	4.20	4.20
B	$-10^\circ \sim 0^\circ, -10^\circ \sim 0^\circ$	-4476.59	58.73	-28.32	-0.04	4.22	4.22
C	$-5^\circ \sim 5^\circ, 125^\circ \sim 135^\circ$	-2585.25	370.86	-382.23	-0.76	17.59	17.61
D	$72^\circ \sim 77^\circ, 20^\circ \sim 40^\circ$	-257.23	45.18	-39.44	-0.06	3.81	3.81
E	$45^\circ \sim 50^\circ, 170^\circ \sim 180^\circ$	-5444.67	29.37	-24.31	-0.03	4.02	4.02

suggest that in mid- and low-latitude regions, the differences between the two models are smaller, indicating overall higher reliability. Considering the orbital inclination of altimetry satellites and their measurement methods, these discrepancies can be attributed to the complexity of geological structures in high-latitude regions. Furthermore, areas near coastlines and shallow waters show greater model differences, increasing the discrepancies between models. The mean values across all latitude intervals approach zero, demonstrating strong global consistency between the two models. This supports the effectiveness of utilizing ~~multi-directional mean sea level~~ multidirectional MSS data for global ~~gradient of gravity anomaly~~ VGGA inversion.

Table 6 examines the impact of seafloor slope on the residual VGGA model. The results show that the STD and RMS values also show an increasing trend with greater slopes. For instance, in regions with slopes less than 1%, the RMS is relatively low at 7.19 E, indicating higher model stability and consistency. However, in areas where the slope exceeds 10%, the RMS increases to 12.32 E, suggesting a decrease in model reliability. This observation indicates that as the seafloor becomes steeper, it introduces more ~~interference factors~~ sources of interference that challenge the reliability of the VGGA inversion. Additionally, in smoother seafloor regions with slopes under 1%, the residuals may become more sensitive to noise or systematic errors in the input data, further explaining the slight increase in STD and RMS values observed in these low-slope regions.

To further validate the study's conclusions, five representative regions were selected for model difference analysis. The topographic information of these regions is presented in Figure 9, providing a comprehensive understanding of the terrain characteristics that may influence model differences.

The selected regions include the open deep-sea area of the South Pacific far from land (Region A), the southeastern Atlantic region near the continental shelf with varied topography (Region B), the area near the Indonesian archipelago with complex seafloor topography (Region C), the high-latitude North Atlantic region near the Arctic Circle (Region D), and the western Pacific deep-sea region characterized by complex underwater terrain ~~but well-covered by satellites~~ and good satellite coverage (Region E). A comparative analysis of these regions explored the effects of offshore distance, latitude, and sea depth on ~~altimetry inversion~~ the accuracy of altimetry inversion, with ~~the~~ statistics provided in Table 7 and modeling results shown in Figure 10.

~~The modeling results in different regions are shown in Figure 10.~~

Region A in the South Pacific (5° S to 5° N, 120° W to 110° W) is located in a remote, open deep-sea area, far from any landmasses or islands. The seafloor topography in this region is predominantly flat, with no significant seamounts or trenches.

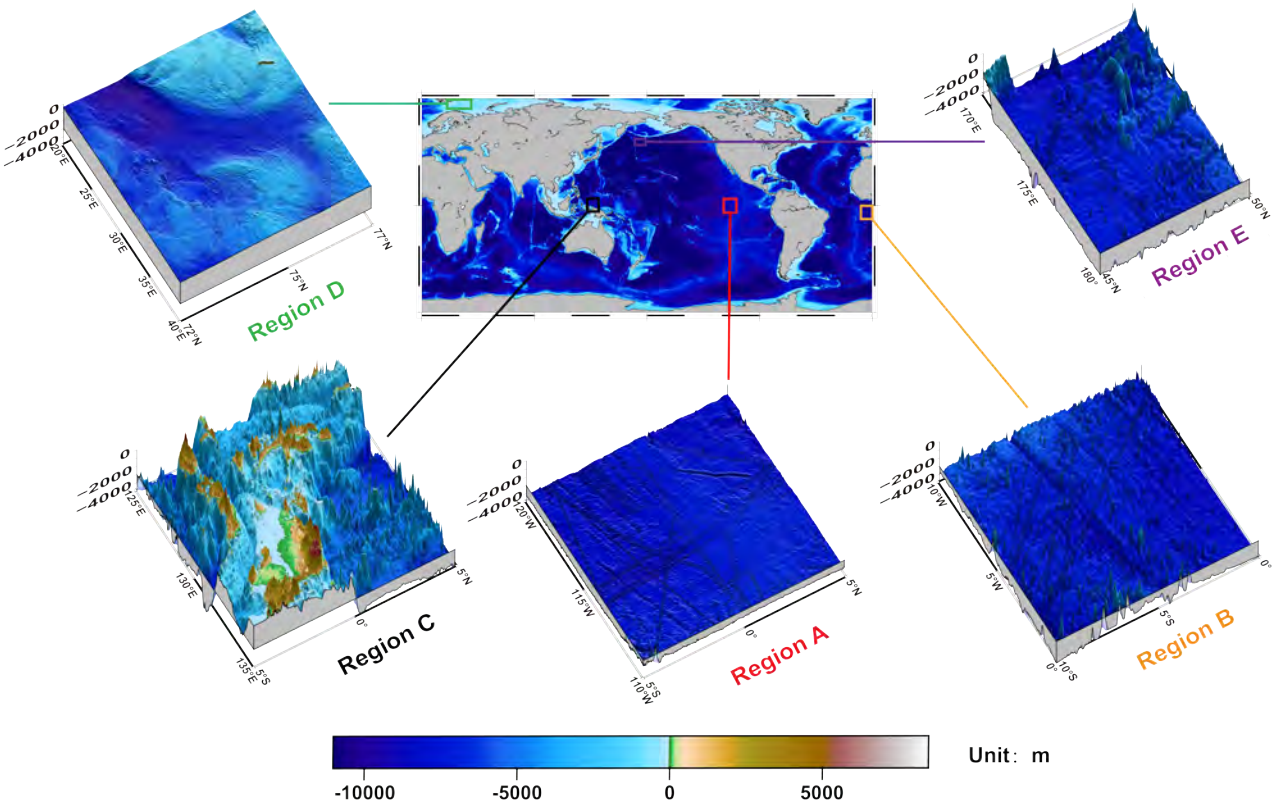

Figure 9. Topographic representation of five selected regions for model difference analysis: (A) the open deep-sea area of the South Pacific far from land, (B) the southeastern Atlantic region near the continental shelf with varied topography, (C) the area near the Indonesian archipelago with complex seafloor topography, (D) the high-latitude North Atlantic region near the Arctic Circle, and (E) the western Pacific deep-sea region characterized by complex underwater terrain but well-covered by satellites.

These conditions create a stable environment for satellite altimetry data inversion, leading to minor residuals between the ~~VGGA~~ SDUSTVGGA and SIO V32.1 models. The low STD and RMS indicate strong consistency between the models in this region. This suggests that, in open ocean areas distant from land, the model performs with high accuracy and stability, likely due to the minimal interference from topographical variations and external factors.

In contrast, Region B in the southeastern Atlantic (10° S to 0°, 10° W to 0°) features varying seafloor topography with an average depth of approximately -4487 meters and is closer to the continental shelf. The seafloor topography ~~here is~~ fig more complex than in Region A. As a result, the residual extremes between the ~~VGGA~~ SDUSTVGGA and SIO V32.1 curv models are significantly larger, with maximum and minimum differences of 58.73 E and -28.32 E, respectively. This indicates that the increased complexity of the seafloor topography introduces greater challenges in the inversion process, resulting in larger discrepancies between the models. These results suggest that in regions with more intricate terrain, satellite altimetry data quality is affected by topographical complexity, resulting in increased uncertainty and decreased model consistency.

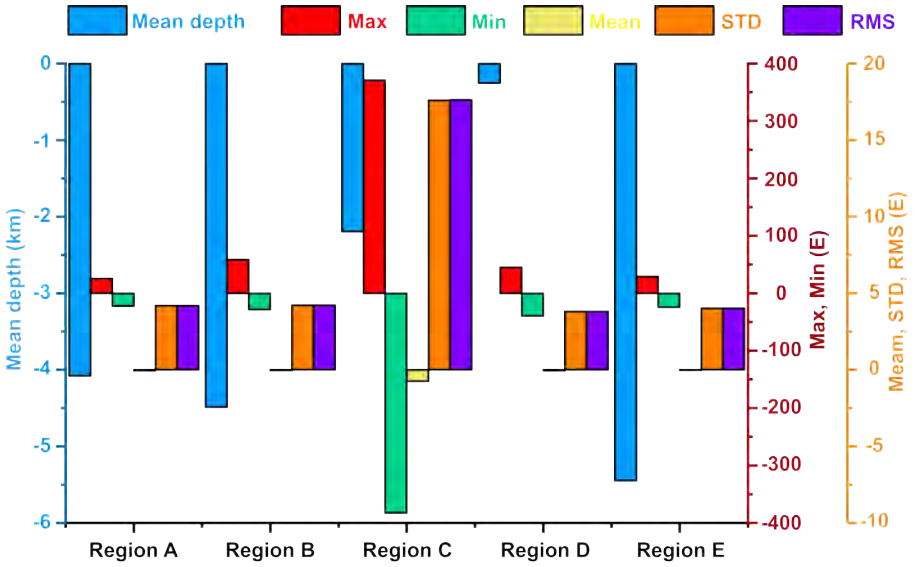

Figure 10. Comparison of differences between the ~~VGGA~~ SDUSTVGGA model and the SIO V32.1 curv model across selected regions. The regions include: (A) a deep-sea area in the South Pacific, (B) a southeastern Atlantic region with varied topography, (C) the Indonesian archipelago with complex seafloor features, (D) the high-latitude North Atlantic near the Arctic Circle, and (E) a western Pacific deep-sea area. The bars represent key metrics such as mean depth, maximum and minimum differences, mean, STD, and RMS of the residuals.

Compared to Regions A and B, the significantly higher ~~residual values~~ residuals in Region C (5° S to 0°, 125° E to 135° E) indicate that the complexity of the seafloor topography, combined with the multipath effect, poses greater challenges for the DTU21 MSS model in low-latitude areas. The steep slopes and varied elevations associated with seamounts and deep trenches introduce greater variability in gravity anomaly signals, complicating the inversion process and decreasing model consistency. As a result, the large residual extremes observed between the ~~VGGA~~ SDUSTVGGA and SIO V32.1 models suggest that satellite altimetry data accuracy in this region is more susceptible to interference from local topographical features. These findings highlight that in low-latitude regions with highly complex terrain structures, the model performance is less reliable compared to relatively flat or less complex regions, as seen in Regions A and B.

Region D in the North Atlantic near the Arctic Circle (72° N to 77° N, 20° E to 40° E) has a relatively smooth seafloor topography with an average shallow depth of approximately -256 meters. Despite its high-latitude location, the region lacks significant topographical undulations or complex structures. These flat conditions result in smaller residuals between the ~~VGGA~~ SDUSTVGGA and SIO V32.1 models, with maximum and minimum differences of 45.18 E and -39.44 E, respectively, and an STD and RMS of 3.81 E. The strong consistency between the models in this region is likely due to stable ocean currents in polar areas and comprehensive satellite coverage.

Region E in the western Pacific deep-sea area (45° N to 50° N, 170° E to 180° E) is characterized by an extremely deep average depth of about -5446 meters. Although the seafloor topography here is relatively complex compared to Region B, Region E benefits from better satellite coverage due to its mid-latitude location. Consequently, the residuals between the

Table 8. Statistical differences obtained by subtracting the SDUSTVGGA model from the curv_SWOT model (unit: E)

Filter Type	Max	Min	Mean	STD	RMS	Exclusion Rate
Raw	1247.19	-1845.47	-0.094	7.952	9.324	-
10σ Filter	79.43	-79.61	-0.116	6.816	8.038	0.07%
3σ Filter	23.76	-23.95	-0.126	5.147	6.167	1.41%

~~VGGA~~ SDUSTVGGA and SIO V32.1 models are relatively small, with maximum and minimum differences of 29.37 E and -24.31 E, respectively. The STD and RMS are 4.02 E, indicating better model performance in this region compared to Region B.

The comparison of these five regions confirms that the DTU21 MSS model effectively manages complex ocean dynamics in deep-sea and high-latitude areas, including regions near polar ice caps, demonstrating its reliability across global oceanic environments. The results indicate that the consistency between the inversion results and the SIO V32.1 model is not directly correlated with sea depth or latitude. Instead, it is the seafloor topography, particularly in shallow-water regions and areas with complex underwater terrain, that leads to instability in satellite altimetry data, which directly affects the consistency between the two models.

~~Due to~~

5.2 Comparison with curv_SWOT and insights from GEBCO

This study conducted two exploratory experiments to evaluate the performance and potential applications of the SDUSTVGGA model. The first experiment involved a direct comparison with the curv_SWOT model, while the second experiment utilized GEBCO bathymetric data to explore potential correlations between VGGA and bathymetric features.

The curv_SWOT model, derived from the SWOT (Surface Water and Ocean Topography) satellite mission, represents a significant advancement in oceanographic research. The SWOT satellite provides high-resolution and wide-coverage observations, which are crucial for capturing fine-scale oceanic phenomena such as eddies and internal tides. However, the current dataset spans only one year, making it a snapshot of short-term oceanic conditions rather than a representation of long-term stable ocean gravity fields. As a result, the curv_SWOT data may contain signals influenced by transient oceanographic phenomena, which could affect its stability and representativeness as a VGGA reference model. The statistical differences between the SDUSTVGGA and curv_SWOT models are summarized in Table 8.

The results in Table 8 reveal significant differences between the SDUSTVGGA and curv_SWOT models. The unfiltered data exhibit a maximum difference of 1247.19 E and a minimum difference of -1845.47 E, with a STD of 7.952 E and a RMS of 9.324 E. These values are notably larger than those observed when comparing SDUSTVGGA with the SIO V32.1 curv model (Table 2), where the maximum and minimum differences were 791.01 E and -673.00 E, respectively, with an STD of 7.24 E and an RMS of 8.50 E. This contrast suggests that the curv_SWOT model has a broader dynamic range and higher variability, likely due to its design for capturing fine-scale oceanic phenomena.

Filtering (10σ and 3σ) reduces the differences between the models, as shown in Table 8. However, the broader trends remain consistent with those observed in Table 2. Extreme outliers in the curv_SWOT data, likely associated with transient phenomena such as mesoscale eddies and internal waves, contribute significantly to the observed discrepancies. These transient signals, while valuable for short-term oceanographic studies, differ from the long-term trends captured by the SDUSTVGGA model.

The comparison with the ~~lack of in-situ VGGA measurements, this study aims to explore alternative methods to validate the performance of the SDUST2023VGGA model(hereafter referred to as SDUSTVGGA). Given that both the~~ SIO V32.1 ~~Curv model and the VGGA model are derived from~~ curv model further highlights the importance of temporal and spatial characteristics in VGGA modeling. The SIO V32.1 curv model, derived from decades of satellite altimetry data, ~~they can partially verify the methodology but not the accuracy of the inversion results. Therefore, in this exploratory attempt, the GEBCO bathymetric model was used~~ reflects averaged oceanographic conditions over a long time period. In contrast, the curv_SWOT model's sensitivity to short-term phenomena results in higher variability and a wider dynamic range. This observation explains why the SDUSTVGGA model aligns more closely with the SIO V32.1 curv model in terms of overall variability and dynamic range.

Given the limitations of the curv model and the lack of in-situ VGGA measurements, this study further explores the potential of using bathymetric data from GEBCO as an alternative ~~reference to assess the SDUSTVGGA model~~validation approach. However, the indirect and weak relationship between bathymetric features and VGGAs has led to relatively low correlation coefficients and ~~R-squared~~ R^2 values, limiting the strength of the conclusions drawn from this analysis. The analysis results, illustrated in Figures 11 and 12, highlight these limitations by separately presenting the correlation analysis (Figure 11) and model performance metrics (Figure 12). Consequently, these results should be interpreted with caution, as the experiment's limitations suggest that the current approach may not fully capture the model's accuracy.

~~The analysis results are illustrated in Figure 11, which shows the correlation coefficients and model performance metrics across different evaluation methods, highlighting the limitations inherent in using bathymetric features as proxies for VGGA validation.~~

~~Spearman rank~~

The correlation analysis revealed weak positive ~~monotonic~~ relationships between the ~~VGGAs predicted by both models and the GEBCO bathymetric data . Kendall's tau showed weak positive relationships, with values of 0.0634 for~~ VGGA data (curv_SWOT, SIO V32.1~~and 0.0696 for VGGA.~~ , SDUSTVGGA) and GEBCO bathymetric features. The Pearson correlation coefficients ~~were slightly higher, at 0.1179 for V32.1 and~~ ranged from 0.0887 to 0.1361~~for VGGA. These results suggest that while the models exhibit some degree of correlation with the bathymetric data, the relationships remain weak , reflecting the models' limited ability~~ , with SDUSTVGGA showing the highest value. Similarly, the Spearman rank correlation coefficients and Kendall's tau values also indicated weak monotonic and ordinal associations, further supporting the limited capacity of these models to capture the ~~complexity of the underlying geophysical processes~~ complex relationships between geophysical processes and bathymetry. These weak correlations may be attributed to inherent differences between bathymetric data and VGGA models, as well as potential measurement errors or the complexity of geophysical processes that are not easily captured by these models.

Figure 11. Correlation ~~and model performance comparisons for different bathymetric and satellite-derived models. Top: Correlation~~ coefficients (Pearson, Spearman, Kendall) between the GEBCO bathymetric model (A) and the ~~SIO V32.1 Curv~~ curv_SWOT model (B), as well as between the GEBCO model (A) and the ~~VGGA model (C), illustrating the weak associations between these datasets. Bottom: R^2 values from various regression models (Linear Regression, Polynomial Regression, SVR, and MLP) applied to compare GEBCO (A) with~~ SIO V32.1 ~~Curv~~ model ~~(B), and GEBCO (A) with VGGA (~~C), ~~demonstrating the impact of non-linear modeling~~ and ~~hyperparameter optimization on improving~~ the SDUSTVGGA model ~~performance~~(D).

Figure 12. Performance comparisons for regression models applied to GEBCO (A) with curv_SWOT (B), SIO V32.1 (C), and SDUSTVGGA (D). R^2 values are shown for Linear Regression, Polynomial Regression, SVR, and MLP methods, where the MLP used three hidden layers (200, 200, 100 neurons) and Deep MLP used seven hidden layers (512, 512, 256, 256, 128, 128, 64 neurons).

~~Both models performed poorly in linear regression, with R-squared values of 0.0139 for V32.1 and 0.0185 for VGGA. These low R-squared values underscore the inability of simple linear modelsto adequately explain the variance in the GEBCO bathymetric data, highlighting the need for more sophisticated, non-linear modeling approaches. Polynomial regression models~~

led to modest improvements in predictive In terms of model performance, regression analysis was conducted using various methods to compare the predictive accuracy of GEBCO with each of the three models. Linear regression models exhibited poor performance, with R-squared values of 0.0221 for V32.1 and 0.0230 for VGGA. While these results suggest that non-linear models can better capture some underlying data patterns, the improvements were still relatively minor, indicating that further refinement is needed R^2 values below 0.02, confirming the inadequacy of simple linear approaches in this context. Polynomial regression models showed slightly better performance, particularly for SDUSTVGGA ($R^2 = 0.3586$), but still fell short of capturing the full complexity of the relationships.

Support Non-linear regression approaches, particularly support vector regression (SVR)was employed to explore the models' capacity to capture non-linear relationships. Initial resultsfrom basic SVR models revealed substantial improvements over linear and polynomial regression, with R-squared values of 0.3619 for V32.1 and , provided significantly better results. The original SVR configurations achieved R^2 values ranging from 0.3586 to 0.3745for VGGA. To further optimize model performance, both grid search and random search techniques were applied. These efforts resulted in higher R-squared values: , with further improvements observed after hyperparameter optimization. The best-performing SVR model achieved an R^2 value of 0.4228 for VGGA and 0.4093 for V32.1 using grid search, and 0.4123 for VGGA and 0.4027 for V32.1 using random search. These improvements underscore the importance of hyperparameter tuningin enhancing model performanceSDUSTVGGA, highlighting the value of non-linear modeling and parameter tuning.

Neural network modelswere also explored to capture more intricate non-linear relationships. A shallow multi-layer perceptron Among the neural network models, the Multi-Layer Perceptron (MLP) model, consisting of two hidden layers with 50 units each, demonstrated further improvement over the SVR models, achieving R-squared values of 0.4454 for V32.1 and with three hidden layers demonstrated the highest performance. The original MLP configuration achieved R^2 values of up to 0.4599 for VGGA. These results surpassed all previous models, suggesting that the shallow MLP was effective at learning complex patterns in the data. SDUSTVGGA, showcasing the ability of neural networks to capture complex non-linear relationships. Hyperparameter optimization provided marginal improvements, with the MLP (Grid) configuration achieving an R^2 value of 0.4594 for SDUSTVGGA. The Deep MLP model, which introduced seven hidden layers, achieved comparable performance, suggesting that additional layers did not lead to overfitting in this case.

However, hyperparameter optimization of the MLP models through grid search and random search did not yield significant improvements. Grid search optimization for MLP models with two hidden layers (50 units each) resulted in R-squared values of 0.4450 for V32.1 and 0.4585 for VGGA, while random search optimization produced similar results, with R-squared values of 0.4453 for V32.1 and 0.4568 for VGGA. These findings indicate that the MLP models' performance did not improve substantially with hyperparameter optimization, suggesting that further tuning or alternative modelarchitectures may be needed.

When deeper neural networks were tested, consisting of three hidden layerswith 100 units each, the performance decreased significantly. The deep MLP models achieved R-squared values of 0.0376 for V32.1 and 0.0416 for VGGA, indicating that the added complexity led to overfitting without providing additional predictive power. These findings suggest that simpler

architectures, such as the shallow MLP, are more suitable for this problem as they balance model complexity with predictive accuracy.

In conclusion, the findings suggest that while deeper neural networks may improve performance in some cases, the shallow MLP model provided the optimal balance between complexity and accuracy for this task. The results emphasize It is worth noting that the curv_SWOT model, derived from short-term satellite observations, showed slightly lower performance compared to the other models. This may be attributed to its sensitivity to transient oceanographic phenomena, which are not representative of long-term stable gravity fields. However, the SWOT satellite's high-resolution and wide-coverage capabilities remain valuable for capturing fine-scale oceanic dynamics. These results underscore the effectiveness of non-linear models, particularly SVR and MLP, in capturing the complex relationships between VGGAs and bathymetric data . While each successive model showed some improvementneural networks in modeling the relationships between bathymetric data and VGGA models. However, the limitations of the current experimental setup must be acknowledged. The weak correlations and relatively low R-squared values indicate that relying solely on VGGA is insufficient due to its indirect relationship with bathymetric features. Introducing additional data might improve correlations or model performance but could also introduce more error, complicating interpretation and reducing robustness. Further refinement and exploration of more advanced techniques are necessary to better capture the complexities inherent in geophysical datausing only VGGA data highlight the need for additional data sources or more sophisticated models to achieve more accurate predictions in future studies.

6 Conclusions

This study used the gridded This study introduces the SDUST2023VGGA, a global VGGA model derived from the DTU21 MSS model , combined with multi-directional MSS data, to develop the global VGGA model, SDUST2023VGGA. The reliability of combined with multidirectional MSS data. The model provides a detailed view of VGGA variations over the global ocean and has been rigorously evaluated against the SDUST2023VGGA model was validated by comparing it with the SIO V32.1 curv model model to ensure its reliability. The results show a global residual mean of -0.08 Eötvös and an RMS of 8.50 E, demonstrating the consistency and accuracy of the SDUST2023VGGA model on a global scale. The comparison confirmed the effectiveness of the proposed method, which considers the complex oceanic environment and effectively suppresses the amplification of geoid uncertainties caused by second-order derivative calculations.

The process starts by dividing the To construct the model, the global oceanic area was divided into multiple sub-regions to address computational limitations. Next, The geoid was derived by subtracting the CNES-CLS22 MDT influence from DTU21 MSS datafrom multiple directions are used, and the influence of CNES-CLS22 MDT is subtracted to derive the geoid. The remove-restore method is then was applied to eliminate the long-wavelength signalsof the gravity field, obtaining the residual geoid. In the third step, the . A weighted least squares method is employed to calculate was used to compute the residual VGGAbased on the residual geoid, after which , which was then combined with the long-wavelength signals are restored to construct the VGGA model within to produce the final VGGA model for each sub-region. Finally, all sub-regions are merged

~~to construct~~ These sub-regional models were merged to form the SDUST2023VGGA model~~(hereafter referred to as VGGA)~~, covering the latitude range from 80° S to 80° N.

~~The VGGA model was compared with~~ Validation against the SIO V32.1 ~~curv model , both derived from satellite altimetry data. The following conclusion can be drawn: On a global scale, the VGGA model, derived through multi-directional sea surface height data inversion, shows a high degree of consistencywith the SIO V32.1 model. In the longitudinal direction, the differences exhibit significant numerical fluctuations without a consistent trend, indicating that the VGGA in this direction is affected by various geographical and geophysical factors. In contrast, in the latitudinal direction, the complexity of topography in high-latitude regions leads to greater discrepancies between the VGGA and~~ model revealed strong global consistency. In open ocean basins with relatively flat terrain, the models showed close agreement, while regions near steep seafloor slopes, complex coastlines, and high latitudes displayed larger discrepancies. These differences highlight the challenges of processing altimetry data in complex regions and the influence of topography on VGGA modeling. Analysis of five selected subregions (A–E) confirmed that the model's consistency with SIO V32.1 ~~models compared to those in mid- and low-latitude regions~~is closely linked to topographical features, validating the robustness of the DTU21 MSS model in addressing complex oceanic and high-latitude conditions.

~~The inversion results are directly affected by coastal proximity and topographical features. In open ocean basins far from the shore with relatively flat terrain, there is a strong consistency between the VGGA and SIO V32.1 models. However, in regions near complex coastal areas, the discrepancies between the models are more pronounced. This is likely due to the influence on satellite altimetry data quality and differences in processing strategies. Indirectly, sea depth also plays a role; in shallow waters, which often correspond to complex coastlines, the consistency between the two models is poor. Conversely, in deep-sea regionswhere the terrain is generally flat, the consistency is significantly better~~Two exploratory experiments were conducted to further assess the SDUST2023VGGA model. The first experiment compared the model with the curv_SWOT dataset, revealing significant differences due to the latter's sensitivity to transient oceanographic phenomena. The second experiment explored correlations between VGGA and GEBCO bathymetric data, showing weak relationships but improved performance with non-linear methods such as SVR and shallow MLP. These results highlight the challenges of using short-term datasets and indirect validation approaches, emphasizing the need for cautious interpretation.

The SDUST2023VGGA model offers a new approach to studying global VGGA, providing improved coverage and reduced uncertainties in long-wavelength geoid estimation. It shows potential for broad applications in geophysical and oceanographic research, particularly in capturing detailed gravity variations across diverse oceanic regions. The model is openly available, encouraging its use in scientific studies and supporting further validation and refinement.

7 Data availability

The datasets used in this study are listed in Table 9, along with their corresponding DOIs and access information.

Table 9. Data availability and DOI information

Dataset	DOI
DTU21MSS	https://doi.org/ 10.11583/DTU.19383221.v1 (Andersen et al., 2023)
CNES-CLS22MDT	https://doi.org/ 10.22541/essoar.170158328.85804859/v1 (Jousset et al., 2023)
XGM2019e	https://doi.org/ 10.5880/ICGEM.2019.007 (Zingerle et al., 2020)
V32.1	https://doi.org/ 10.1126/science.1258213 (Sandwell et al., 2014; Garcia et al., 2014)
GEBCO2024	https://doi.org/ 10.5285/1c44ce99-0a0d-5f4f-e063-7086abc0ea0f (GEBCO Bathymetric Compilation Group 2024, 2024)

Calculations in this study utilized the ICGEM service (Ince et al., 2019), which was used to compute the long-wavelength component of the vertical gradient of gravity anomaly (VGGA). The service can be accessed at https://icgem.gfz-potsdam.de/tom_longtime.

The SDUST2023VGGA, is available at the Zenodo repository (https://doi.org/10.5281/zenodo.14177000 (Zhou et al., 2024)). This model includes global ocean VGGA in NetCDF format (latitude vector, longitude vector, and VGGA matrix).

Author contributions. Ruichen Zhou and Jinyun Guo contributed equally to the conceptualization and design of the study. Ruichen Zhou conducted the primary investigation, data curation, formal analysis, and wrote the original draft of the manuscript. Jinyun Guo supervised the project, provided resources, and contributed significantly to the methodology and manuscript revision. Shaoshuai Ya was involved in data acquisition and supported data analysis. Heping Sun offered technical support, guidance, and contributed to software development. Xin Liu performed validation and contributed to the review and editing of the manuscript. All authors have read and approved the final version of the manuscript.

Competing interests. The authors declare that they have no conflict of interest.

Disclaimer. The views expressed in this article are those of the authors and do not necessarily reflect the views of their affiliated institutions.

Acknowledgements. The authors express their appreciation to DTU (Technical University of Denmark), CNES (Centre National d'Études Spatiales), TUM (Technical University of Munich), SIO (Scripps Institution of Oceanography), and GEBCO (General Bathymetric Chart of the Oceans) for their commitment to open data policies. The availability of high-quality, accessible datasets from these institutions significantly advances geosciences, enabling researchers worldwide to conduct robust and innovative studies. We also thank the International Centre for Global Earth Models (ICGEM) service team for their efforts in providing and maintaining global gravity field models, which greatly facilitated this research.

Additionally, we acknowledge the contributions of all cited authors. Figures in this study were generated using the Generic Mapping Tools ~~(Wessel et al., 2019)~~(Wessel et al., 2019), which greatly facilitated the visualization and interpretation of results. GMT was developed by Pål Wessel, Professor of Geophysics at the University of Hawai'i at Mānoa, and his colleagues. We extend our deepest gratitude to the late Professor Wessel for his invaluable contributions to the scientific community, particularly in the field of geosciences.

This study was partially supported by the National Natural Science Foundation of China (grant Nos. 42430101, 42192535, and 42274006). We are grateful for the valuable feedback provided by the reviewers.

References

Ablain, M., Legeais, J. F., Prandi, P., Marcos, M., Fenoglio-Marc, L., Dieng, H. B., Benveniste, J., and Cazenave, A.: Satellite Altimetry-Based Sea Level at Global and Regional Scales, Surveys in Geophysics, 38, 7–31, https://doi.org/10.1007/s10712-016-9389-8, 2017.

Álvarez, O., Giménez, M., Klinger, F. L., Folguera, A., and Braitenberg, C.: The Peru-Chile Margin from Global Gravity Field Derivatives, pp. 59–79, Springer International Publishing, Cham, ISBN 978-3-319-67774-3, https://doi.org/10.1007/978-3-319-67774-3_3, 2018.

Andersen, O. B. and Knudsen, P.: DNSC08 mean sea surface and mean dynamic topography models, Journal of Geophysical Research: Oceans, 114, C11 001, https://doi.org/10.1029/2008JC005179, 2009.

Andersen, O. B., Rose, S. K., Abulaitijiang, A., Zhang, S., and Fleury, S.: The DTU21 global mean sea surface and first evaluation, Earth System Science Data, 15, 4065–4075, https://doi.org/10.5194/essd-15-4065-2023, 2023.

Annan, R. F., Wan, X., Hao, R., and Wang, F.: Global marine gravity gradient tensor inverted from altimetry-derived deflections of the vertical: CUGB2023GRAD, Earth System Science Data, 16, 1167–1176, https://doi.org/10.5194/essd-16-1167-2024, 2024.

Bouman, J., Bosch, W., and Sebera, J.: Assessment of Systematic Errors in the Computation of Gravity Gradients from Satellite Altimeter Data, Marine Geodesy, 34, 85–107, https://doi.org/10.1080/01490419.2010.518498, 2011.

Butler, D. K.: Microgravimetric and gravity gradient techniques for detection of subsurface cavities, Geophysics, 49, 1084–1096, https://doi.org/10.1190/1.1441723, 1984.

Clift, P. and Vannucchi, P.: Controls on tectonic accretion versus erosion in subduction zones: Implications for the origin and recycling of the continental crust, Reviews of Geophysics, 42, RG2001, https://doi.org/https://doi.org/10.1029/2003RG000127, 2004.

DiFrancesco, D., Grierson, A., Kaputa, D., and Meyer, T.: Gravity gradiometer systems-Advances and challenges, Geophysical Prospecting, 57, 615–623, https://doi.org/10.1111/j.1365-2478.2008.00764.x, 2009.

Escartín, J., Smith, D. K., Cann, J., Schouten, H., Langmuir, C. H., and Escrig, S.: Central role of detachment faults in accretion of slow-spreading oceanic lithosphere, Nature, 455, 790–794, https://doi.org/10.1038/nature07333, 2008.

Fu, L.-L. and Cheney, R. E.: Application of satellite altimetry to ocean circulation studies: 1987–1994, Reviews of Geophysics, 33, 213–223, https://doi.org/10.1029/95RG00187, 1995.

Fuchs, M. J., Bouman, J., Broerse, T., Visser, P., and Vermeersen, B.: Observing coseismic gravity change from the Japan Tohoku-Oki 2011 earthquake with GOCE gravity gradiometry, Journal of Geophysical Research: Solid Earth, 118, 5712–5721, https://doi.org/10.1002/jgrb.50381, 2013.

Garcia, E. S., Sandwell, D. T., and Smith, W. H.: Retracking CryoSat-2, Envisat and Jason-1 radar altimetry waveforms for improved gravity field recovery, Geophysical Journal International, 196, 1402–1422, https://doi.org/10.1093/gji/ggt469, 2014.

GEBCO Bathymetric Compilation Group 2024: The GEBCO_2024 Grid - a continuous terrain model of the global oceans and land, NERC EDS British Oceanographic Data Centre NOC, https://doi.org/10.5285/1c44ce99-0a0d-5f4f-e063-7086abc0ea0f, dataset: The GEBCO_2024 Grid is a global continuous terrain model for ocean and land with a spatial resolution of 15 arc seconds. The dataset is developed through the Nippon Foundation-GEBCO Seabed 2030 Project., 2024.

Guo, J., Gao, Y., Hwang, C., and Sun, J.: A multi-subwaveform parametric retracker of the radar satellite altimetric waveform and recovery of gravity anomalies over coastal oceans, Science China Earth Sciences, 53, 610–616, https://doi.org/10.1007/S11430-009-0171-3, 2010.

Han, S., Carbotte, S. M., Canales, J. P., Nedimović, M. R., and Carton, H.: Along-Trench Structural Variations of the Subducting Juan de Fuca Plate From Multichannel Seismic Reflection Imaging, Journal of Geophysical Research: Solid Earth, 123, 3122–3146, https://doi.org/https://doi.org/10.1002/2017JB015059, 2018.

Hao, R., Wan, X., and Annan, R. F.: Enhanced Short-Wavelength Marine Gravity Anomaly Using Depth Data, IEEE Transactions on Geoscience and Remote Sensing, 61, 5903 109, https://doi.org/10.1109/TGRS.2023.3242967, 2023.

Hofmann-Wellenhof, B. and Moritz, H.: Physical Geodesy, Springer Vienna, ISBN 978-3-211-33545-1, 2006.

Hu, M., Zhang, S., Jin, T., Wen, H., Chu, Y., Jiang, W., and Li, J.: A new generation of global bathymetry model BAT_WHU2020, Acta Geodaetica et Cartographica Sinica, 49, 939–954, https://doi.org/10.11947/j.AGCS.2020.20190526, 2020.

Hwang, C.: A bathymetric model for the South China Sea from satellite altimetry and depth data, Marine Geodesy, 22, 37–51, https://doi.org/10.1080/014904199273597, 1999.

Hwang, C., Kao, E.-C., and Parsons, B.: Global derivation of marine gravity anomalies from Seasat, Geosat, ERS-1 and TOPEX/POSEIDON altimeter data, Geophysical Journal International, 134, 449–459, https://doi.org/10.1111/j.1365-246X.1998.tb07139.x, 1998.

Hwang, C., Cheng, Y., Han, J., Kao, R., Huang, C., Wei, S., and Wang, H.: Multi-Decadal Monitoring of Lake Level Changes in the Qinghai-Tibet Plateau by the TOPEX/Poseidon-Family Altimeters: Climate Implication, Remote Sensing, 8, 446, https://doi.org/10.3390/rs8060446, 2016.

Ince, E. S., Barthelmes, F., Reißland, S., Elger, K., Förste, C., Flechtner, F., and Schuh, H.: ICGEM – 15 years of successful collection and distribution of global gravitational models, associated services, and future plans, Earth System Science Data, 11, 647–674, https://doi.org/10.5194/essd-11-647-2019, 2019.

Jousset, S., Mulet, S., Wilkin, J., Greiner, E., Dibarboure, G., and Picot, N.: New global Mean Dynamic Topography CNES-CLS-22 combining drifters, hydrological profiles and High Frequency radar data, in: Proceedings of the Ocean Surface Topography Science Team (OSTST) 2022 Meeting, https://doi.org/10.24400/527896/a03-2022.3292, 2022.

Jousset, S., Mulet, S., Greiner, E., et al.: New Global Mean Dynamic Topography CNES-CLS-22 Combining Drifters, Hydrological Profiles and High Frequency Radar Data, ESS Open Archive, https://doi.org/10.22541/essoar.170158328.85804859/v1, 2023.

Khaki, M., Forootan, E., Sharifi, M., Awange, J., and Kuhn, M.: Improved gravity anomaly fields from retracked multimission satellite radar altimetry observations over the Persian Gulf and the Caspian Sea, Geophysical Journal International, 202, 1522–1534, https://doi.org/10.1093/gji/ggv240, 2015.

Kim, S.-S. and Wessel, P.: New global seamount census from altimetry-derived gravity data, Geophysical Journal International, 186, 615–631, https://doi.org/10.1111/j.1365-246X.2011.05076.x, 2011.

Knudsen, P., Andersen, O., and Maximenko, N.: A new ocean mean dynamic topography model, derived from a combination of gravity, altimetry and drifter velocity data, Advances in Space Research, 68, 1090–1102, https://doi.org/j.asr.2019.12.001, 25 Years of Progress in Radar Altimetry, 2021.

Knudsen, P., Andersen, O. B., Maximenko, N., and Hafner, J.: A New Combined Mean Dynamic Topography Model – DTUUH22MDT, Presented at ESA Living Planet Symposium 2022, poster presentation, 2022.

Li, Z., Guo, J., Zhu, C., Liu, X., Hwang, C., Lebedev, S., Chang, X., Soloviev, A., and Sun, H.: The SDUST2022GRA global marine gravity anomalies recovered from radar and laser altimeter data: contribution of ICESat-2 laser altimetry, Earth System Science Data, 16, 4119–4135, https://doi.org/10.5194/essd-16-4119-2024, 2024.

Marks, K. M., Smith, W., and Sandwell, D.: Significant improvements in marine gravity from ongoing satellite missions, Marine Geophysical Research, 34, 137–146, https://doi.org/10.1007/s11001-013-9190-8, 2013.

Melini, D. and Piersanti, A.: Impact of global seismicity on sea level change assessment, Journal of Geophysical Research: Solid Earth, 111, B03 406, https://doi.org/10.1029/2004JB003476, 2006.

Michael, P. J. and Cornell, W. C.: Influence of spreading rate and magma supply on crystallization and assimilation beneath mid-ocean ridges: Evidence from chlorine and major element chemistry of mid-ocean ridge basalts, Journal of Geophysical Research: Solid Earth, 103, 18 325–18 356, https://doi.org/https://doi.org/10.1029/98JB00791, 1998.

Moritz, H.: Advanced Physical Geodesy, Sammlung Wichmann : Neue Folge : Buchreihe, Wichmann, ISBN 9780856261954, 1980.

Mortimer, Z.: Gravity Vertical Gradient Measurements for the Detection of Small Geologic and Anthropogenic Forms; discussion, Geophysics, 42, 1484–1485, https://doi.org/10.1190/1.1440812, 1977.

Muhammad, S., Zulfiqar, A., and Muhammad, A.: Vertical gravity anomaly gradient effect of innermost zone on geoid-quasigeoid separation and an optimal integration radius in planar approximation, Applied Geomatics, 2, 9–19, https://doi.org/10.1007/s12518-010-0015-z, 2010.

Novák, P., Tenzer, R., Eshagh, M., and Bagherbandi, M.: Evaluation of gravitational gradients generated by Earth's crustal structures, Computers & Geosciences, 51, 22–33, https://doi.org/10.1016/j.cageo.2012.08.006, 2013.

Oruç, B.: Edge Detection and Depth Estimation Using a Tilt Angle Map from Gravity Gradient Data of the Kozaklı-Central Anatolia Region, Turkey, Pure and Applied Geophysics, 168, 1769–1780, https://doi.org/10.1007/s00024-010-0211-0, 2011.

Panet, I., Pajot-Métivier, G., Greff-Lefftz, M., Métivier, L., Diament, M., and Mandea, M.: Mapping the mass distribution of Earth's mantle using satellite-derived gravity gradients, Nature Geoscience, 7, 131–135, https://doi.org/10.1038/ngeo2063, 2014.

Pavlis, N. K., Holmes, S. A., Kenyon, S. C., and Factor, J. K.: The development and evaluation of the Earth Gravitational Model 2008 (EGM2008), Journal of Geophysical Research: Solid Earth, 117, B04 406, https://doi.org/10.1029/2011JB008916, 2012.

Poland, M. P. and Carbone, D.: Insights into shallow magmatic processes at Kīlauea Volcano, Hawai'i, from a multiyear continuous gravity time series, Journal of Geophysical Research: Solid Earth, 121, 5477–5492, https://doi.org/10.1002/2016JB013057, 2016.

Rao, D. G., Krishna, K. S., Neprochnov, Y. P., and Grinko, B. N.: Satellite gravity anomalies and crustal features of the Central Indian Ocean Basin, Current Science, 86, 948–957, http://www.jstor.org/stable/24109277, 2004.

Romaides, A. J., Battis, J. C., Sands, R. W., Zorn, A., Jr, D. O. B., and DiFrancesco, D. J.: A comparison of gravimetric techniques for measuring subsurface void signals, Journal of Physics D: Applied Physics, 34, 433–443, https://doi.org/10.1088/0022-3727/34/3/331, 2001.

Rummel, R., Yi, W., and Stummer, C.: GOCE gravitational gradiometry, J. Geodesy, 85, 777–790, https://doi.org/10.1007/s00190-011-0500-0, 2011.

Sandwell, D. T.: Antarctic marine gravity field from high-density satellite altimetry, Geophysical Journal International, 109, 437–448, https://doi.org/10.1111/j.1365-246X.1992.tb00106.x, 1992.

Sandwell, D. T. and Smith, W. H. F.: Marine gravity anomaly from Geosat and ERS 1 satellite altimetry, Journal of Geophysical Research: Solid Earth, 102, 10 039–10 054, https://doi.org/10.1029/96JB03223, 1997.

Sandwell, D. T. and Smith, W. H. F.: Global marine gravity from retracked Geosat and ERS-1 altimetry: Ridge segmentation versus spreading rate, Journal of Geophysical Research: Solid Earth, 114, B01 411, https://doi.org/10.1029/2008JB006008, 2009.

Sandwell, D. T. and Smith, W. H. F.: Slope correction for ocean radar altimetry, Journal of Geodesy, 88, 765–771, https://doi.org/10.1007/s00190-014-0720-1, 2014.

Sandwell, D. T., Smith, W. H. F., Gille, S., Kappel, E., Jayne, S., Soofi, K., Coakley, B., and Géli, L.: Bathymetry from space: Rationale and requirements for a new, high-resolution altimetric mission, Comptes Rendus. Géoscience, 338, 1049–1062, https://doi.org/10.1016/j.crte.2006.05.014, 2006.

Sandwell, D. T., Müller, R. D., Smith, W. H. F., Garcia, E., and Francis, R.: New global marine gravity model from CryoSat-2 and Jason-1 reveals buried tectonic structure, Science, 346, 65–67, https://doi.org/10.1126/science.1258213, 2014.

Schwatke, C., Dettmering, D., Bosch, W., and Seitz, F.: DAHITI – an innovative approach for estimating water level time series over inland waters using multi-mission satellite altimetry, Hydrology and Earth System Sciences, 19, 4345–4364, https://doi.org/10.5194/hess-19-4345-2015, 2015.

Silvestrin, P., Aguirre, M., Massotti, L., Leone, B., Cesare, S., Kern, M., and Haagmans, R.: The Future of the Satellite Gravimetry After the GOCE Mission, in: Geodesy for Planet Earth, pp. 223–230, Springer Berlin Heidelberg, 2012.

Skourup, H., Farrell, S. L., Hendricks, S., Ricker, R., Armitage, T. W. K., Ridout, A., Andersen, O. B., Haas, C., and Baker, S.: An Assessment of State-of-the-Art Mean Sea Surface and Geoid Models of the Arctic Ocean: Implications for Sea Ice Freeboard Retrieval, Journal of Geophysical Research: Oceans, 122, 8593–8613, https://doi.org/10.1002/2017JC013176, 2017.

Smith, W. H. F. and Sandwell, D. T.: Global Sea Floor Topography from Satellite Altimetry and Ship Depth Soundings, Science, 277, 1956–1962, https://doi.org/10.1126/science.277.5334.1956, 1997.

Stray, B., Lamb, A., Kaushik, A., Vovrosh, J., Rodgers, A., Winch, J., Hayati, F., Boddice, D., Stabrawa, A., Niggebaum, A., Langlois, M., Lien, Y.-H., Lellouch, S., Roshanmanesh, S., Ridley, K., de Villiers, G., Brown, G., Cross, T., Tuckwell, G., Faramarzi, A., Metje, N., Bongs, K., and Holynski, M.: Quantum sensing for gravity cartography, Nature, 602, 590–594, https://doi.org/10.1038/s41586-021-04315-3, 2022.

Sulistioadi, Y. B., Tseng, K.-H., Shum, C. K., Hidayat, H., Sumaryono, M., Suhardiman, A., Setiawan, F., and Sunarso, S.: Satellite radar altimetry for monitoring small rivers and lakes in Indonesia, Hydrology and Earth System Sciences, 19, 341–359, https://doi.org/10.5194/hess-19-341-2015, 2015.

van der Meijde, M., Pail, R., Bingham, R., and Floberghagen, R.: GOCE data, models, and applications: A review, International Journal of Applied Earth Observation and Geoinformation, 35, 4–15, https://doi.org/10.1016/j.jag.2013.10.001, 2015.

Vermeer, M. and Rahmstorf, S.: Global sea level linked to global temperature, Proceedings of the National Academy of Sciences, 106, 21 527–21 532, https://doi.org/10.1073/pnas.0907765106, 2009.

Vignudelli, S., Birol, F., Benveniste, J., Fu, L.-L., Picot, N., Raynal, M., and Roinard, H.: Satellite Altimetry Measurements of Sea Level in the Coastal Zone, Surveys in Geophysics, 40, 1319–1349, https://doi.org/10.1007/s10712-019-09569-1, 2019.

Vigouroux, N., Williams-Jones, G., Chadwick, W., Geist, D., Ruiz, A., and Johnson, D.: 4D gravity changes associated with the 2005 eruption of Sierra Negra volcano, Galápagos, Geophysics, 73, WA29–WA35, https://doi.org/10.1190/1.2987399, 2008.

Wan, X., Annan, R. F., and Ziggah, Y. Y.: Altimetry-Derived Gravity Gradients Using Spectral Method and Their Performance in Bathymetry Inversion Using Back-Propagation Neural Network, Journal of Geophysical Research: Solid Earth, 128, e2022JB025 785, https://doi.org/10.1029/2022JB025785, 2023.

Wang, B., Li, T., Deng, Z., and Fu, M.: Wavelet Transform Based Morphological Matching Area Selection for Underwater Gravity Gradient-Aided Navigation, IEEE Transactions on Vehicular Technology, 72, 3015–3024, https://doi.org/10.1109/TVT.2022.3218998, 2023.

Wessel, P., Luis, J. F., Uieda, L., Scharroo, R., Wobbe, F., Smith, W. H. F., and Tian, D.: The Generic Mapping Tools Version 6, Geochemistry, Geophysics, Geosystems, 20, 5556–5564, https://doi.org/https://doi.org/10.1029/2019GC008515, 2019.

Yu, Z., Zhao, D., and Li, J.: Structure and dynamics of the Tonga subduction zone: New insight from P-wave anisotropic tomography, Earth and Planetary Science Letters, 598, 117 844, https://doi.org/10.1016/j.epsl.2022.117844, 2022.

Yuan, J., Guo, J., Zhu, C., Li, Z., Liu, X., and Gao, J.: SDUST2020 MSS: a global $1' \times 1'$ mean sea surface model determined from multi-satellite altimetry data, Earth System Science Data, 15, 155–169, https://doi.org/10.5194/essd-15-155-2023, 2023.

Zhou, R., Liu, X., Li, Z., Sun, Y., Yuan, J., Guo, J., and Ardalan, A. A.: On performance of vertical gravity gradient determined from CryoSat-2 altimeter data over Arabian Sea, Geophysical Journal International, 234, 1519–1529, https://doi.org/10.1093/gji/ggad153, 2023.

Zhou, R., Guo, J., Ya, S., Sun, H., and Liu, X.: SDUST2023VGGA, https://doi.org/10.5281/zenodo.14177000, 2024.

Zhu, C., Guo, J., Yuan, J., Li, Z., Liu, X., and Gao, J.: SDUST2021GRA: global marine gravity anomaly model recovered from Ka-band and Ku-band satellite altimeter data, Earth System Science Data, 14, 4589–4606, https://doi.org/10.5194/essd-14-4589-2022, 2022.

Zingerle, P., Pail, R., Gruber, T., and Oikonomidou, X.: The combined global gravity field model XGM2019e, Journal of Geodesy, 94, 66, https://doi.org/10.1007/s00190-020-01398-0, 2020.